The Role of Boron in Phosphorescence Persistence of Rare-Earth Co-activated Alkalai Aluminates

By

Murat GokhanEskin

Submitted to the Graduate School of Engineering and Natural Sciences in partial fulfillment of the requirements for the degree of Master of Science

Sabancı University
Spring 2011

THE ROLE OF BORON IN PHOSPHORESCENCE PERSISTENCE OF RARE-EARTH CO-ACTIVATED ALKALAI ALUMINATES

APPROVED BY

Asst. Prof. Cleva Ow-Yang ……..

(Dissertation Supervisor)

Assoc. Prof. Sondan Durukanoglu Feyiz ……..

Prof. Dr. Hasan Mandal ……..

Asst Prof. Burc Misirlioglu ……..

Asst. Prof. Ayse Turak ……..

DATE OF APPROVAL ……..

Abstract

Rare-earth co-doped (Eu, Dy) $SrAl_4O_7$ (SA_2ED) phosphor powders were synthesized by using a modified Pechini process. It has been noted that the addition of boron has two impacts on these phosphors—the persistence duration is extended, and the processing of phase pure powders is facilitated. Thus the objective of this thesis work is to investigate the effect of boron on SA_2ED phosphors. Varying amounts of boron were incorporated into the SA_2 lattice to investigate the effects on crystal structure and optical properties. X-ray diffraction spectra showed that boron addition enhances the phase purity of the powder at a calcination temperature of 1000 °C, whereas the formation of a new S_4A_7 phase was induced when a calcination temperature of 1100 °C was used. The afterglow duration was extended to longer than 5 hours when boron was present in 5-30 mol%. To elucidate the enhanced optical properties, interband trap characteristics were studied by thermoluminescence and photoluminescence. Moreover, to understand the structure-property relationship via investigating the electronic structure of the boron inside the crystal, ELNES studies were performed. With ELNES fingerprinting and quantitative analysis of the ELNES data, information on local bonding of boron and its effects on the crystal lattice were investigated.

Özet

Nadir toprak elementleriyle (Eu, Dy) katkilandirilmis $SrAl_4O_7$(SA_2ED) fosforlu tozlari Pechini teknigi kullanilarak sentezlenmistir. Eklenen boronun bu fosforlar uzerinde 2 etkisi oldugu tespit edilmistir: fosforışıllık suresinin uzamasi ve fazin saf bir sekilde elde edilmesini kolaylastirmasi. Sonuc itibariyle bu tezin amaci boronun SA_2ED fosforlarina olan etkisinin arastirilmasidir. Degisen miktarlarda boron SA_2 kristal yapisi icerisine, boronun kristal yapiya ve optik ozelliklere olan etkisinin arastirilmasi icin yerlestirilmistir X-isini kirilim spektralari gostermistir ki boron eklenmesi, 1000 ^oC'de kalsine edilen tozlarin fazlarinin saflasmasini kolaylastirmis, 1100 ^oC'de kalsine edilenlerde ise yeni bir S_4A_7 fazinin olusmasina sebep olmustur. Fosforışıllık suresi 5-30 mol % boron koyuldugunda 5 kata kadar artmaktadir. Gelisen optik ozelliklerin daha iyi anlasilabilmesi icin bant-arasi tuzak karakteristikleri termoluminesans ve fotoluminesans olcumleriyle arastirilmistir. Ayrica, yapi-ozellik iliskisinin kristal matriks icindeki boronun elektronik yapisi incelenerek anlasilabilmesi icin ELNES calismalari yapilmistir. ELNES bulgularinin nicel ve nitel analizleri ile boronun bolgesel bag kurmasi ve bunun kristal yapiya olan etkisine dair bilgi edinilmistir.

Acknowledgements

First and foremost, I would like to thank my thesis advisor Prof. Cleva Ow-Yang for her support, motivation, patience and wisdom she shared with me throughout my master's studies. Apart from the theoretical background she provided with, she also taught how to do science and how to scientifically approach problems that I encounter during my studies. Furthermore, I had the chance to work with great scholars, attended workshops about the state of the art topics and visited research facilities which are foremost institutes in their fields as a result of her efforts in providing me with a better education.

I also would like to thank my co-advisor Prof. Mehmet Ali Gulgun for his vast knowledge of ceramics and lab experience and also the motivation and support. He was the reason for my choosing materials science at the end of my sophomore year and I think I will be thankful to him for the rest of my life. Together with Prof. Cleva Ow-Yang, the academic insight and environment he gave was priceless. I will always consider them as my academic parents (!).

I also would like to thank my senior student and dear friend Halil Selman Onsel for his devoted efforts in our project. He spent days in front of the TL instrument to extract a few drops of data which was significantly important for us.

Many thanks to Prof. Saso Sturm from Josef Stefan Institute, Ljubljiana, Slovenia for his time and efforts on TEM analysis of our powders. I also want to thank Alenka Lenart and Kristina Zagar for their hospitality during our visits to Slovenia.

The research leading to these results has received funding from the [European Community's] [European Atomic Energy Community's] Seventh Framework Programme ([/FP7/2007-2013/] [/FP7/2007-2011/]) under /grant agreement /n° 233484.

I would like to thank Dr. Vesna Srot and Prof. Peter van Aken from Max Planck Institute for Intelligent Systems, Stuttgart, Germany for their experience, time and knowledge in analysis of our powders in the VG STEM. I also acknowledge the European Union for support under the IP3 project ESTEEM (Enabling Science and Technology through European Electron Microscopy).

Many thanks to Veli Bayir for the ICP analysis, Hasan Kurt and Guliz Inan for their helps in PL and TL characterizations as well as their supports and friendship.

I warmly thank my colleagues in SU, Cem Burak Kılıç, Taner Aytun, Özlem Kocabaş, Sinem Taş, Firuze Okyay, Elif Özden, Fatih Melemez, Burcu Özel, Burcu Saner, Selime Shawuti, Melike Mercan Yıldızhan, Erim Ülkümen, Hale Nur Cologlu, Mustafa Baysal, Ayça Abakay and Kaan Bilge for building a pleasant research environment.

Special thanks to my parents, mom and dad for their endless supports tolerance and prays and also my dearest sister whose help and support I felt in every aspect of life.

Special thanks to Elif Nihal Ates for indirectly (!) inspiring me in my research, feeding me with motivation and love.

I also acknowledge the TUBITAK BIDEB 2210 Master's Scholarship Program for their generous scholarship throughout my Master's studies.

Table of Contents

List of Figures

List of Tables

List of Abbrevations

CA Citric acid

CB Conduction band

EDS Energy dispersive X-ray spectroscopy

EDX Energy dispersive X-ray

EELS Electron energy loss spectroscopy

EG Ethylene glycol

ELNES Energy Loss Near Edge Spectroscopy

EXELFS Extended electron-energy loss fine structure

FL Fluoroscence

PL Photoluminescence

TEM Transmission electron microscopy

TL Thermoluminescence

UV Ultraviolet

VB Valence band

XRD X-ray diffraction

ZLP Zero loss peak

Eg Band gap energy

$(SrO)_x(Al_2O_3)_y\ S_xA_y$

CHAPTER 1. INTRODUCTION

While phosphors have traditionally played an important role in lighting technology, more recent developments in long persistence aluminate host materials have been realized in safety lighting, such as back-up solutions for power outages. Alkaline earth aluminates, $MAl_2O_4:Eu^{2+}$ (M = Ca, Sr) have distinctive optical properties which makes them good candidates for such applications. They are odorless and nonflammable powders and usually pale yellow in color. Being chemically and biologically inert, they are safe to use in many applications. Furthermore, activated with a suitable dopant (eg. europium, dysprosium), they are significantly efficient phosphors with long afterglow durations and brightness [1, 2].

The optical properties of strontium aluminate are much superior to its predecessor, copper-activated zinc sulfide. About 10 times more brightness and afterglow duration were reported [3, 4, 5, 6].

The emission from strontium aluminate phosphors are either green or aqua hue depending on the host and dopants. It was reported that green gives the highest brightness and aqua the longest afterglow duration [3, 4, 5, 6]. The excitation occurs mostly by the UV light; the wavelengths range from 200 to 450 nm. The wavelength for green emission is 520nm, the blue-green emission is at 505nm, and the blue emission is at 490nm.

The emission color, intensity and duration strongly depend on the crystal structure of the material. Phosphorescence is the delayed (~10 ns or longer) emission of light during the de-excitation of an electron. Whereas short afterglow duration would be sufficient for conventional lighting applications, extended phosphorescence would enable broader use of energy-efficient safety lighting, including garments worn by relief workers and larger area building surfaces. Boron oxide is a common sintering flux and was used in the production of alkali aluminate phosphors by conventional solid state reaction. In 2003, Nag and Kutty noted that the presence of B was associated with persistence of over hours in Eu^{2+} and

Dy^{3+} co-doped strontium aluminate (SA) powders [3]. However, the role of B in dramatically enhancing the afterglow duration is still unknown.

In previous work by our group [3, 7], we have demonstrated a solution polymerization method for producing boron-incorporated, Eu^{2+} and Dy^{3+} co-doped $SrAl_4O_7$ (SA_2ED), with enhanced afterglow persistence and intensity. Beyond merely the optical properties, surprisingly high amounts of boron could be incorporated into the SA lattice. To clarify how boron is entering into the doped SA_2ED lattice and the nature of its impact on the phosphorescence duration, the crystal structure and electronic structure have been investigated.

Rare earth ions have been used as dopants in phosphors to create optical centers which introduce new energy levels positioned in the energy gap of the crystal [21, 27, 28]. There are transitions between such levels that create new optical bands which do not occur in the original host prior to doping. One of the most common activators used in phosphors: Eu has the following configuration [20-29]:

Eu: $1s^2\ 2s^2\ 2p^6\ 3s^2\ 3p^6\ 4s^2\ 3d^{10}\ 4p^6\ 5s^2\ 4d^{10}5p^6\ 6s^2\ 4f^7$.

The 4f electrons of trivalent Eu^{3+} cation are shielded by 5s and 5p outer electrons because 5s2 and 5p6 are less energetic configurations. Due to this shielding, these 4f levels are less affected from the ligand atoms.

When Eu first enters the lattice, it has a 3+ charge and the configuration is:

Eu^{3+}: $1s^2\ 2s^2\ 2p^6\ 3s^2\ 3p^6\ 4s^2\ 3d^{10}\ 4p^6\ 5s^2\ 4d^{10}5p^6\ 4f^6$.

In order to maintain phosphorescence, Eu^{3+} should be reduced to Eu^{2+}, shifting its configuration to:

Eu^{2+}: $1s^2\ 2s^2\ 2p^6\ 3s^2\ 3p^6\ 4s^2\ 3d^{10}\ 4p^6\ 5s^2\ 4d^{10}5p^6\ 4f^7$.

However, after this reduction, the e^- density distribution is deformed and the symmetry is lifted around the Eu atom. Breaking symmetry lifts degeneracy and this causes the electronic levels to rearrange. Now, there are two energy levels for Eu^{2+}.

$Eu^{2+} + hv \rightarrow Eu^{2+}*$

The high energy configuration then becomes:

$Eu^{2+}*$: $1s^2\ 2s^2\ 2p^6\ 3s^2\ 3p^6\ 4s^2\ 3d^{10}\ 4p^6\ 5s^2\ 4d^{10}5p^6\ 4f^6\ 5d^1$.

Vanya (master thesis, 2008) reported that [13] addition of Dy extends the phosphorescence in strontium aluminate phosphors. Such an effect might be a result of nonradiative energy transfer as described in Garcia Sole's book: An Introduction to the Optical Spectroscopy of Inorganic Solids.

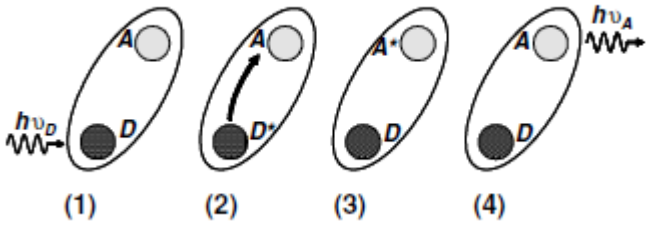

Figure 1.1Sequential steps for a nonradiative energy transfer process [22].

The D center is called the donor and can be created by addition of activators such as Eu, Dy, Sb and Mn. When the donor absorbs the excitation light $h\nu_D$, it shifts to an excited state D* as seen in Figure 1.1: (2). This excited donor center transmits its energy to an acceptor "A" via relaxing to its ground state, shifting the acceptor to an excited state "A*" (3). It is the acceptor which emits its characteristic radiation $h\nu_A$ while relaxing to its ground state.

Such kind of an energy transfer is employed to increase the efficiency of commercial phosphor $Ca_5(PO_4)_3$ (FCl), which is doubly activated by Sb^{3+} and Mn^{2+} ions. When it is activated only by Mn^{2+}, the efficiency is so low because of the weak absorption bands of the divalent Mn^{2+} ion. When it is co-activated with Sb^{3+} ion, a very intense emission is produced. Because Sb^{3+} ion (donors) absorbs the UV emission from the Hg atoms inside the fluorescent tube and then transfer some of this energy to Mn^{2+} ion (acceptor). Apart from the structural changes, a similar process might be the case for Dy^{2+} ions interacting with Eu ions inside the strontium aluminate crystal.

Our main goal is to design phosphorescent materials with long afterglow duration, high emission intensity and a low manufacturing cost. Boron incorporation into the SA host lattice increases the afterglow duration and the emission intensity. If we can understand the mechanism for extended phosphorescence as well as the structure-property relationship, boron can decrease the amount of Eu and Dy rare-earth dopants lower the manufacturing costs significantly. Therefore, the goal of this thesis is to find out "The Role of Boron in Phosphorescence Persistence of Rare-Earth Co-activated Alkalai Aluminates".

1.1 THEORY

1.1.1 Electron Energy Loss Spectroscopy

Electromagnetic lenses of a TEM can be used to focus the beam into a very small diameter (1nm-0.1nm), it is called a probe and a spatial resolution on the order of atomic dimensions is acquired. When this probe interacts with the specimen, some of the energy will be lost due to inelastic scattering as the beam gets through the specimen to the detector. Electron energy-loss spectroscopy (EELS) measures the energy distribution of electrons that encounters such an energy loss at the end of this beam-specimen interaction.

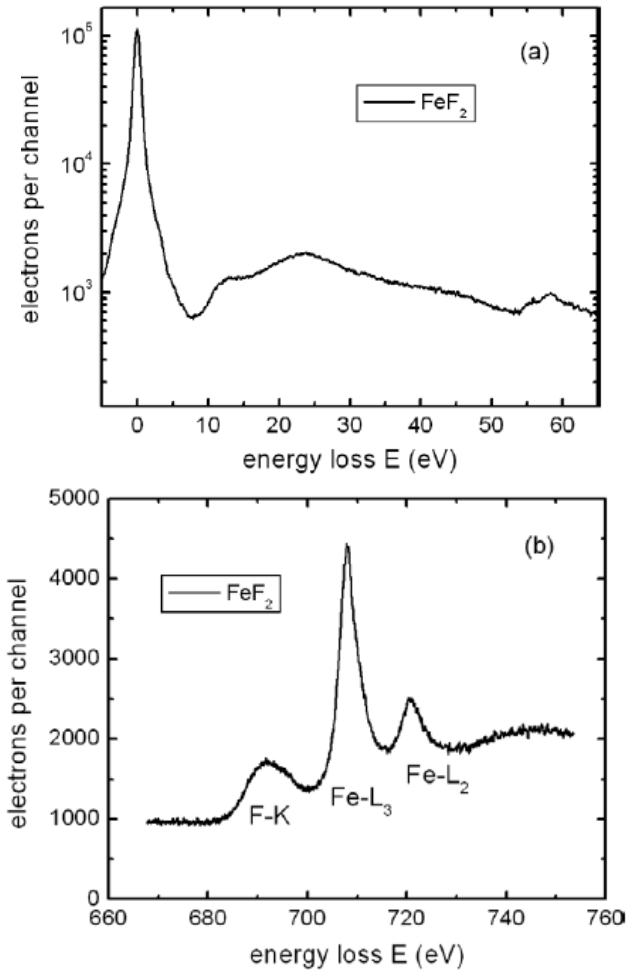

Figure 1.2 Energy-loss spectrum of an iron fluoride film: (a) low-loss region with a logarithmic intensity scale and (b) part of the core-loss region, with linear vertical scale [8].

Figure 1.2(a) is a typical energy-loss spectrum recorded up to a few tens of electron volts. This part of the spectrum is called the low-loss region. Some electrons from the beam goes directly through the specimen, experiencing either no interaction with the electrons of the specimen (inelastic scattering) or limited interaction with the atomic nuclei (elastic scattering) and therefore almost no energy loss. The first most intense peak at 0 eV is the zero-loss peak formed by these lossless electrons. The width of the zero-loss peak, typically 0.2–2 eV, corresponds to the energy distribution of the electron source.

Inelastic scattering by valence electrons causes the low-loss features to appear. The plasma resonance of the valence electrons causes a broad, distinctive peak at around 22 eV in Figure 1.2(a). Inelastic scattering by inner-shell electrons appears as an increase in

intensity at around 54 eV, which corresponds to the M_2 and M_3 subshells of iron atoms in this case. The characteristic shape, first a rapid rise and then a broader fall, is termed an ionization edge. In Figure 1.2(b), other ionization edges are shown at higher energy loss.

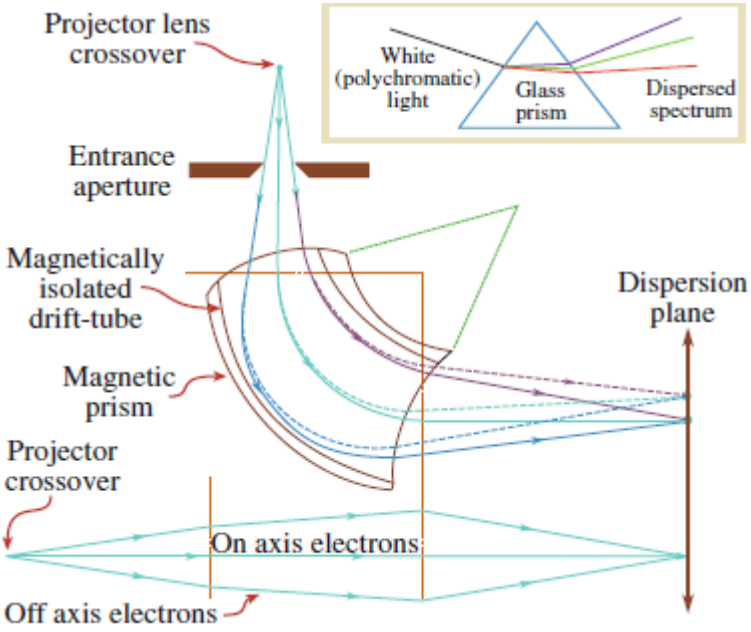

Figure 1.3 Dispersive and focusing properties of a magnetic prism (a) in a plane perpendicular to the magnetic field and (b) parallel to the field. Solid lines represent zero-loss electrons (E = 0); dashed lines represent those that have lost energy during transmission through the specimen [9].

Figure 1.3 shows a magnetic prism which is the main component for TEM-EELS instrumentation. A uniform magnetic field on the order of 0.01 T is generated by the magnetic prism and this field bends electrons into a circular path of radius R, leading to a deflection through an angle of typically 90°. Within this field, electrons follow circular paths of radius R and are deflected through an angle of typically 90°.

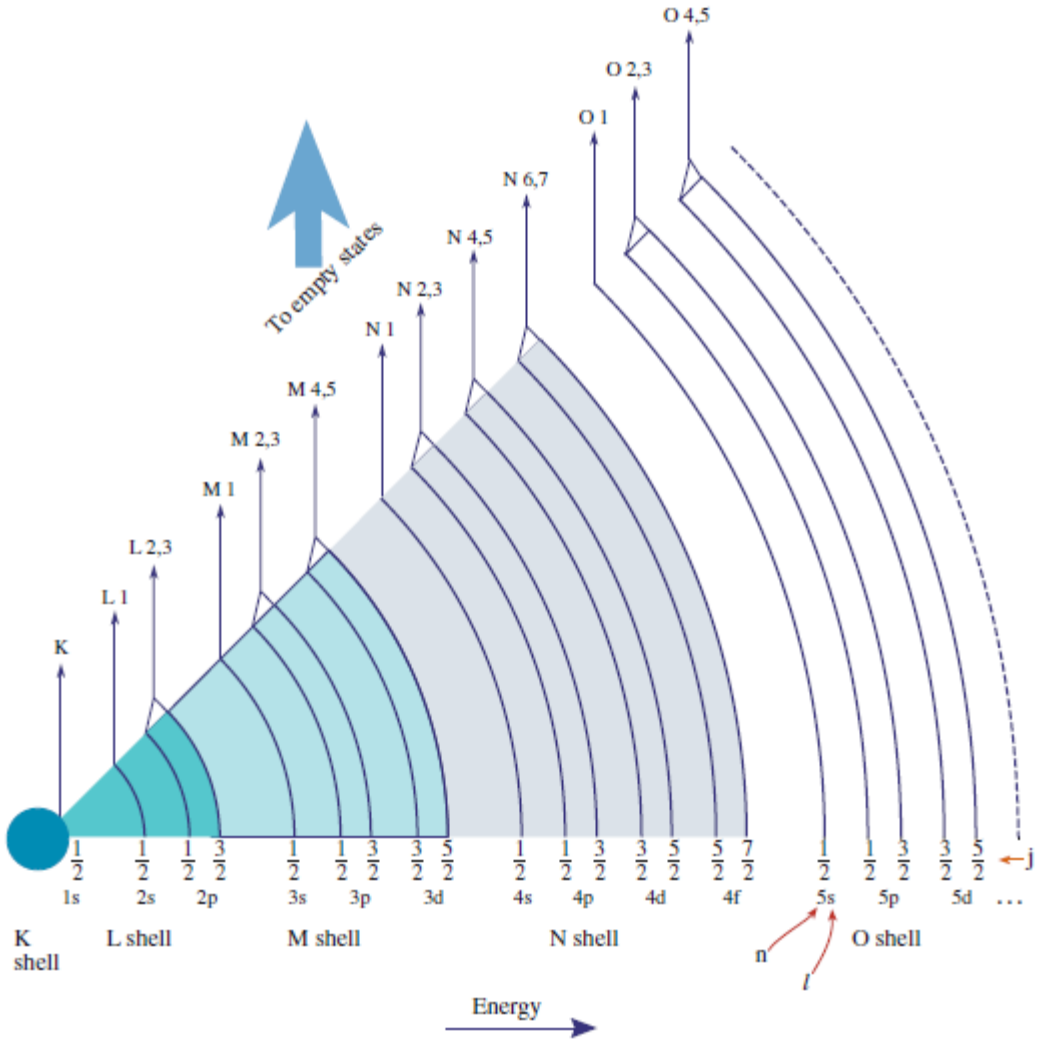

Figure 1.4 The full range of possible edges in the energy-loss spectrum due to core-shell ionization and the associated nomenclature [9].

Figure 1.4 shows the atomic electrons in the inner shells (labeled K, L *etc*. from the nucleus outwards) have binding energies that vary between hundreds and thousands of electron volts. When they are excited by the electron beam, electrons from the lower shells are knocked out to outer shells or ionized, giving rise to ionization edges in the energy-loss spectrum. Since core-electron binding energies are characteristic of each element and each type of shell, the ionization edges can be used to identify which elements are present in the specimen, which is called a "fingerprint". They occur superimposed on a background that represents energy loss due to valence electrons (for example, the high-energy tail of a plasmon peak) or ionization edges of lower binding energy. This background contribution can be extrapolated and removed for quantitative elemental or structural analysis.

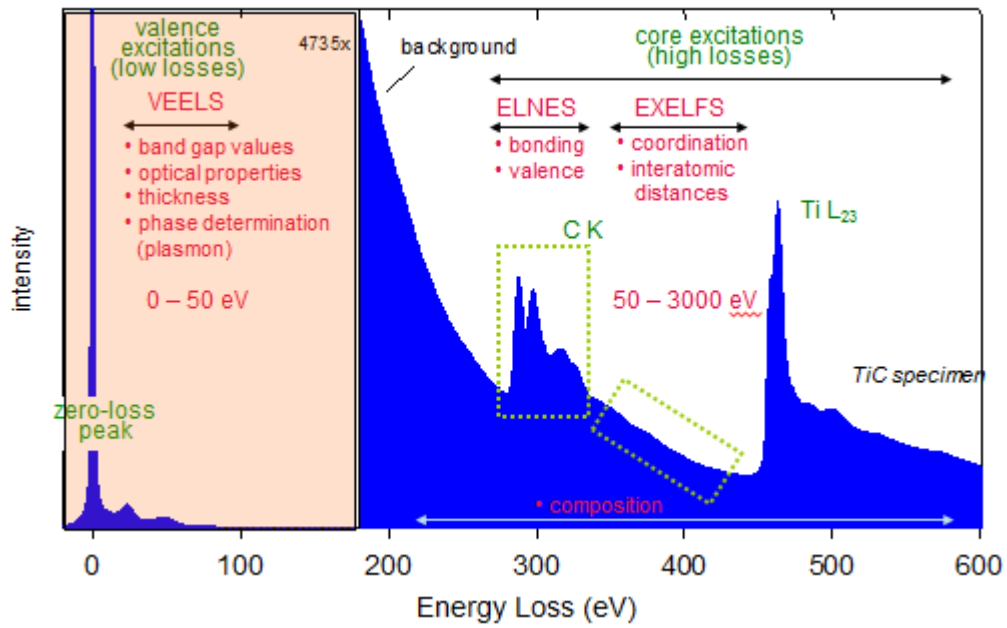

Figure 1.5 A complete EELS spectrum with the regions labeled.

The edge may also show fine structure oscillations within ~50 eV of ionization energy (Figure 1.5), which are due to local bonding effects. This region is called the electron energy-loss near-edge spectrum (ELNES). More than 50 eV after the edge, small intensity oscillations may be detectable, due to diffraction effects from the atoms surrounding the ionized atom, and these are called extended energy-loss fine structure (EXELFS).

As a result, electron energy loss spectroscopy (EELS) is a powerful tool for investigating local bonding and coordination information, because the near edge structure is determined by subtle changes in bonding between nearest neighbor atoms. When this atom exists in different numbers and spatial arrangements in the crystal, the shape of the ELNES will show the characteristic differences that can be interpreted as the coordination fingerprints. Furthermore, if the atom being investigated occurs in several coordinations in the crystal matrix, the near edge structure is a superposition of the corresponding ELNES fingerprints and a quantitative analysis reveals the true nature of the local bonding of the atoms of interest.

1.1.2 Phosphorescence Mechanism and Thermoluminescence

Luminescence is the emission of light during the de-excitation of an electron, and may also be viewed as a form of cold body radiation. The energy in a crystal is stored due to the absorption of light, which may excite an electron into a higher energy, allowed state. If this luminescence occurs during excitation, it is called fluorescence, whereas it is phosphorescence if light emission begins with a delay of at least 10 nanoseconds after extinguishing the excitation.

The presence of structural defects or impurity atoms (or activators in general) serve as trap states or recombination centers for de-exciting electrons and directly affects the ability of the host material to store radiation energy. When de-excitation is stimulated by transferring thermal energy into the host material, the emission is called thermoluminescence (TL), and the spectra contain information on the electronic structure of crystals and the effects of activators on the structure and the dynamic processes of de-excitation. Therefore analysis of the thermoluminescence spectra and of the phosphorescence glow decay curves will provide invaluable information about the kinetics and therefore the structure [10].

In this chapter, some of the existing models explained in the Furetta's review paper [11] for TL measurements will be studied, as well as the mathematical treatment behind them. Quantitative analysis methods for TL data will be mentioned in the results and discussion part.

1.1.2.1 Models for Thermoluminescence

1.1.2.1.1 Halperin and Braner Model

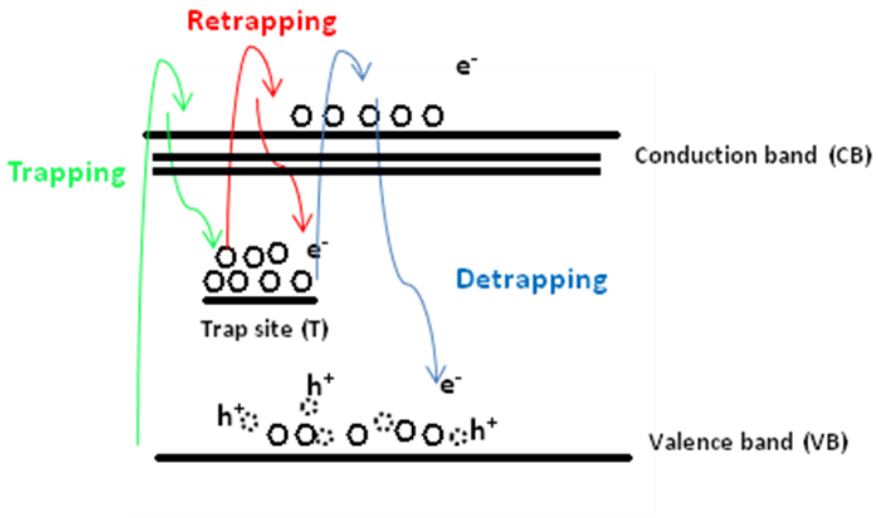

Figure 1.6 Energy band model for the equations proposed by Halperin and Braner

Halperin and Braner proposed a model for the electronic structure of a luminescent material that consists of two bands of allowed energies, the valence and conduction bands, separated by a forbidden energy gap, which contains intermediate electronic trapping states. The most weakly bound valence electrons can be excited into states with energy at the bottom of the conduction band, where they behave like free electrons. During de-excitation, the free electrons may return to the ground state directly by recombining with a hole in the valence band and emitting a photon. However, the electrons may also become trapped by an intermediate energy level trap state first, before eventually recombining with a hole to produce photon emission of a longer wavelength than the energy absorbed for excitation. The difference, *E*, between the bottom of the conduction band (CB) and the trap energy level, *T*, is called the activation energy or the trap depth. It is also possible for the trapped electron to absorb enough energy to transition to a higher energy state, before becoming re-trapped at the intermediate trap state or at a recombination center. Depending on the model, the recombination center may have an energy either near the top of the VB or just above the VB edge in the band gap.

In the Figure 1.6, which is a simple model used for theoretical treatment of a single TL peak, there are 3 different mechanisms shown:

1) Trapping: When a valence band electron is excited to the conduction band, the lifetime of these electrons is short, they will fall back and recombine with holes but if there are metastable states in the forbidden gap like trap states, these electrons can be trapped.

2) De-trapping: If there is enough energy around (*i.e.*, thermal energy at room temperature), these trapped electrons can be excited to the conduction band and then recombine with holes in the valence band.

3) Re-trapping: Not all of the electrons can make it to the valence band for the de-trapping case above. Some of the electrons can again be trapped in the trapped sites while they are falling back to recombine with holes in the valence band.

In this model, 6 parameters were used to quantify the thermoluminescence mechanisms:

N : concentration of trap states in the band gap (cm^{-3})

n: the concentration of electrons in traps (cm^{-3})

$\mathbf{n_c}$: the concentration of free electrons in the conduction band (cm^{-3})

$\mathbf{A_m}$: the recombination probability ($cm^3\,sec^{-1}$)

$\mathbf{A_n}$: the re-trapping probability ($cm^3\,sec^{-1}$)

m: the concentration of holes in recombination centers (cm^{-3})

The energy E was defined as the trap depth or the activation energy above. In other words, it is the energy required to de-trap an electron in T (trap state). For the mathematical treatment, we have to modify the Arrhenius equation, which is used for describing the temperature dependence of the reaction rate of a chemical reaction. The electrons in the trap will have a Maxwellian distribution of thermal energies:

Probability that a trapped electron will escape from a trap per second: $s\exp(-E/k_BT)$, where k_B is Boltzmann's constant, T is the absolute temperature in degrees K.

$I = -\,dm/dt = A_m m n_c$ **Eqn. 1**

$-dn/dt = sn\exp(-E/k_BT) - A_n(N-n)n_c$ **Eqn. 2**

$dn_c/dt = dm/dt - dn/dt$. **Eqn. 3**

$I = -\,dm/dt = A_m m n_c$. This equation suggests that the intensity of *a glow curve is a function of the rate of change in the hole concentration*, since recombination always involves a hole in the valence band, regardless of the source of the electron, be it from the conduction band or from a trap site. The intensity is also correlated to the total number of free electrons recombining with holes (n_c m), multiplied by the recombination probability (A_m), because not all of the free electrons will experience recombination. In order to match the units, A_m should be a function of time here.

$-dn/dt = sn\exp(-E/k_BT) - A_n(N-n)n_c$. This second equation suggests that *the rate of change in the concentration of trapped electrons is a function of the thermal energy* introduced to the system. With the first term, the multiplier $sn\exp(-E/k_BT)$ means only those who can have at least k_BT amount of energy will pass because the term $s\exp(-E/k_BT)$ is the probability that a trapped electron will escape from a trap. Multiplied by the n, $sn\exp(-E/k_BT)$gives the total number of trapped electrons that would experience de-trapping. However, while some of the trapped electrons are de-exciting back into the valence band, electrons from the conduction band may be trapped at this trap state, which will affect the rate of change in the concentration of trapped electrons. The term $(N-n)n_c$ represents the total number of electrons, which were previously in the conduction band and have the potential to de-excite to the available empty trap states ($N-n$) However, it should be noted that not all of them will be trapped at these trap states. There is a probability for them to recombine and $A_n(N-n)n_c$ counts for the total number of conduction band electrons which fall and get trapped into the trap sites. And A_n is a function of time again.

$dn_c/dt = dm/dt - dn/dt$. It would be much clearer if we rearrange this equation as such: $dn_c/dt + dn/dt = dm/dt$. This is now quite obvious that the rate of change in the total number of holes (dm/dt) is equal to the rate of change in the total number of trapped electrons

(dn/dt) plus the rate of change in the total number of electrons in the conduction band (dn_c/dt).

In order to be able to solve these equations, there should be some assumptions to make the situation clearer. First, we can assume that the number of electrons in the conduction band does not change so much, instead it is the number of trapped electrons, which are changing significantly as a function of time. In other words, the electron and hole activity in the trapped sites is dominant. So:

$|dn_c/dt| << |dn/dt|$ which suggests $n_c << n$

Then **eqn.3**: $dn_c/dt = dm/dt - dn/dt$ and so $dn_c/dt + dn/dt = dm/dt$ becomes $dn/dt = dm/dt$.

$dn/dt = dm/dt$ =>**eqn.2**: $- dn/dt = sn\exp(-E/k_BT) - A_n(N-n)n_c = - dm/dt = I = A_m m n_c$ (**eqn.1**).

If we rearrange the equation above:

$sn\exp(-E/k_BT) = A_m m n_c + A_m m n_c => n_c = sn\exp(-E/k_BT) / [A_n(N-n) + A_m m]$

Insert this n_c into **eqn.1** :

$I = sn\exp(-E/k_BT)\, A_m m / [A_n(N-n) + A_m m]$ **Eqn.4**

Eqn.4 gives the TL intensity.

1.1.2.1.2 Randall-Wilkins Model

In the Randall and Wilkins model, retrapping is assumed to be negligible. Consequently, $A_m m >> A_n(N-n)$, which suggests that the trapped electrons at trap states most probably de-excite directly back to the valence band, instead of being re-excited to the conduction band and becoming re-trapped. Then, **eq.4** reduces to:

$I = sn\,exp(-E/k_BT)\, A_m m / [\sout{A_n(N-n)} + A_m m]$ =>

$I = - dm/dt = sn\,exp(-E/k_BT)$ the regular first order case. **Eqn.5**

1.1.2.1.3 Garlick and Gibson Model

Garlick and Gibson assumed that for an electron escaping from a trap state can either recombine with a hole or be retrapped; considering that the recombination rate is identical to the de-trapping rate which means that two probabilities are equal. Thus, if d*n*/d*t* = d*m*/d*t*, then all of the electrons that recombine with holes are those trapped at the trap states. Also, because of charge neutrality, n = m .Additionally, predominating retrapping is assumed by Garlick and Gibson: $A_m m << A_n(N-n)$ because in a TL curve, there is still some TL intensity even after the T_{Max} value. If there were no retrapping at all, there should not be any TL intensity observed after a certain temperature, the intensity should fall dramatically beyond this temperature. This assumption suggests that the electrons trapped at trap states will most probably be re-excited to the conduction band, fall back to the trap states and get trapped again, rather than just falling back to the valence band and recombine with holes. They also assumed that saturation is not the case, which is N >> n which suggests that there will be always available empty trap states. The **eq.4** will reduce to:

$I = sn\exp(-E/k_BT)\, A_m m/ [A_n(N- \cancel{n}) + \cancel{A_m m}] = I = sn\exp(-E/k_BT)\, A_m m/ [A_n N]$ and change m to n:

$I = sn^2\exp(-E/k_BT)\, A_m/ (A_n N)$ (rearranged): $I = n^2\exp(-E/k_BT)\, sA_m/ (A_n N)$ which forms the Garlick and Gibson approximation:

$I = -dn/dt = s'n^2\exp(-E/k_BT)$ where $s' = sA_m/ (A_n N)$. the regular second order case. **eq.6**

The second order kinetics term is used to describe a process where retrapping occurs too.

1.1.2.1.4 Effects of Re-trapping on the Glow Curve Shape

The glow peak shape becomes more symmetrical with the inclusion of re-trapping, as shown in Figure 1.7, suggesting that more de-trapping is occurring at temperatures above

the TL intensity maximum. Additionally, peak temperature increases by 1% when re-trapping is also accounted for, in contrast to without.

It was already mentioned above that the second order kinetics term is used to describe a process where retrapping is considered too whereas it is not in the first order kinetics. Because of this retrapping, the release of electrons due to additional thermal energy is delayed and as a result, the light is emitted even at temperatures above T_M for the second order case.

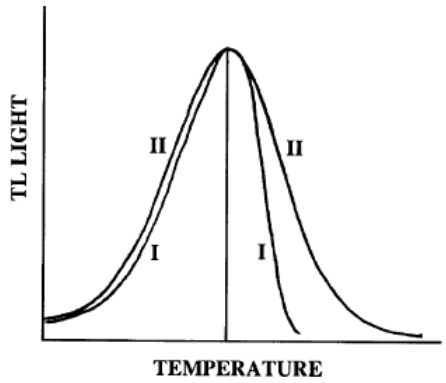

Figure 1.7 Kinetic order effect on the glow curve shape [11].

CHAPTER 2. EXPERIMENTAL

The technique used to synthesize the strontium aluminate powders is the solution polymerization process, also known as the "Pechini method" [12]. It is considered to be the easiest and most versatile sol-gel technique, since the requirements are minimal such as inexpensive chemicals, a few beakers, a magnetic stirrer, a hot plate and a furnace. The technique also does not require an inert atmosphere or strict control over gel processing time and conditions, and it is not sensitive to humidity in the environment.

The method is a kind of polyesterification reaction. Multifunctional organic acids such as citric acid (CA) are used to chelate metal ions to form stable complexes. A diol such as ethylene glycol (EG) is utilized as a solvent during the formation of this complex. EG later works in the polyesterification that ends up with a polymer network with the incorporated metal complexes.

The original Pechini method involves dissolution of CA in EG, prior to mixing the appropriate metal precursors into the EG + CA solution. The temperature is then increased to 100-130°C to ease the polyester formation as a result of the reaction between the EG and CA. After the gel formation, the excess EG is removed via heat-treating the remaining substance at 450-600°C [12].

However, in this work a modified version of Pechini method is employed. Generally, the method described by Vanya Uluc in her thesis was adopted with some minor modifications by the author, Murat Gokhan Eskin. [13].

2.1 Chemicals

Table 2. 1 Chemical List used for SA synthesis.

Name	Chemical Formula	Molecular Weight (g/mol)	Supplier
Aluminium nitrate nonahydrate	$Al(NO_3)_3.9H_2O$	375	Merck
Strontium Nitrate anhydrous	$Sr(NO_3)_2$	211,62	Riedel de-Haer
Europium (III) nitrate hexahydrate	$Eu(NO_3)_3.6H_2O$	445,96	Fluka
Dysprosium (III) nitrate pentahydrate	$Dy(NO_3)_3.5H_2O$	438,5	Fluka
Boron oxide	B_2O_3	69,62	Alfa Aesar
Citric acid monohydrate	$C_6H_8O_7$	210,14	Merck
Ethylene Glycol	$C_2H_6O_2$	62	Carlo Erba

The chemicals used in the synthesis are presented in Table 2.1. Europium (III) nitrate and boron oxide are highly hygroscopic, so they should be kept in a desiccators, and the weighing process should be as quick as possible in order to maintain accurate stoichiometry.

2.1.1 Calculation of the Amounts to be Used

The author used the calculations previously described by Uluc [13]. An Inductively Coupled Plasma Mass Spectroscopy (ICP) analysis was performed on the samples to see the effect of the type of the crucible used but the results also revealed that the measured weight percentages of B amounts were much lower than those calculated. We realized that calculations described in Ref. [13] assumes that SA_2 formation occurs first, and then the co-dopants enters into the SA_2 lattice. However, all the precursors are added simultaneously into the solvent and the co-doping should occur at the same time as the SA_2 lattice forms.

Table 2.2 The excel calculations and entered values for SA_2 co-doped with Eu, Dy and B (Yellow cells are the parameters that should be entered).

	A	B	C	D	E	F	G	H	I	J	K
1											
2											
3		Molecular weight (g/mol)									
4	$Sr(NO_3)_2$	211.62			Amounts used		Mass (gr)	moles			
5	$Al(NO_3)$ 3.9H_2O	375				$SrAl_4O_7$ED	1	G5/B11			
6	$Eu(NO_3)$ 3.6H_2O	445.96			$Sr(NO_3)_2$		H5*B4	H5			
7	$Dy(NO_3)$3.5H_2O	438.5			$Al(NO_3)$ 3.9H_2O		H7*B5	4*H6			
8	B_2O_3	69.62			$Eu(NO_3)$ 3.6H_2O		(H5/100)*H8*B6	1	desired amount for mol %		
9	CA	210.14			$Dy(NO_3)$3.5H_2O		(H5/100)*H9*B7	1	desired amount for mol %		
10	EG	62			B_2O_3		H10*(H5/100)*B8	20	desired amount (Boron percentage)		
11	$SrAl_4O_7$:EDB	((H8*A13+H9*B13+H10*C13)+(100-SUM(H8:H10))*D13)/100			CA		H11*B9	H5*5.5			
12	Eu	Dy	B	$SrAl_4O_7$	EG		H12*B10	H5*5			
13	151.96	162.5	10.81	307.62							
14											

	A	B	C	D	E	F	G	H	I	J	K
1											
2											
3		Molecular weight (g/mol)									
4	$Sr(NO_3)_2$	211.62			Amounts used		Mass (gr)	moles			
5	$Al(NO_3)$ 3.9H_2O	375				$SrAl_4O_7$EDB	1	0.004077			
6	$Eu(NO_3)$ 3.6H_2O	445.96			$Sr(NO_3)_2$		0.862874	0.004077			
7	$Dy(NO_3)$3.5H_2O	438.5			$Al(NO_3)$ 3.9H_2O		6.116203	0.01631			
8	B_2O_3	69.62			$Eu(NO_3)$ 3.6H_2O		0.018184	1	desired amount for mol %		
9	CA	210.14			$Dy(NO_3)$3.5H_2O		0.01788	1	desired amount for mol %		
10	EG	62			B_2O_3		0.056775	20	desired amount (Boron percentage)		
11	$SrAl_4O_7$:EDB	245.2502			CA		4.712616	0.022426			
12	Eu	Dy	B	$SrAl_4O_7$	EG		1.264015	0.020387			
13	151.96	162.5	10.81	307.62							
14											

As seen in Table 2.2, the calculations were performed in order to maintain the stoichiometric ratio. In the cell B10, the molecular weight of SA_2 co doped with Eu, Dy and B (SA_2:EDB) is a dynamic value, which changes according to the Eu, Dy and B mol percentages. Then, the mole numbers of each precursor is calculated according to their stoichiometric ratio in the SA_2 lattice. Cell H5 is the mole number of 1 gr of SA_2:EDB (It should be noted that the cell G5 is also a variable). For example, since 1 mole of $SrAl_4O_7$ is composed of 1 mole of Sr, mole number of $Sr(NO_3)_2$ should be the same as that of SA_2:EDB.

2.2 Procedure

Step 1:

About 250 mL of double distilled, deionized water is boiled for 10 minutes to get rid of the dissolved CO_2. A magnetic stirrer is used to generate a moderate vortex. The weighing of

the $Sr(NO_3)_2$, $Al(NO_3)_3.9H_2O$, CA and EG were performed via using small plastic disposable containers. For the rest of the chemicals aluminum foil was used, because they are hygroscopic. They are measured in very small amounts, and the aluminum folio needs to be dipped into the solution in order to ensure that all of the chemicals weighed were added into the boiling water. The chemicals were added in the following order:

1- $Al(NO_3)_3.9H_2O$

2- $Sr(NO_3)_2$

3- $Eu(NO_3)_3.6H_2O$

4- $Dy(NO_3)_3.5H_2O$

5- B_2O_3

6- CA ($C_6H_8O_7$)

7- EG ($C_2H_6O_2$)

After the addition of these precursors, the solution is stirred for 10 minutes.

Step 2:

The solution is put into a box furnace at 110°C, so that the gelation starts and the evaporation process finishes earlier. Setting this temperature to 110°C instead of 80°C (as described in Ref. [13]) speeds up the process 4 times and the resulting crystal structure is exactly the same.

Step 3:

At the end of evaporation, a white-yellowish substance is produced. It is then ground in a clean agate mortar and put into an alumina crucible. This substance is highly hygroscopic and should be treated in 5-7 minutes, because after 7 minutes it becomes wet and sticky. In

summer, this duration is no longer than 5 minutes, so everything else should be prepared in advance to minimize exposure to the atmosphere.

After grinding, the crucible is placed into a box furnace and heated up to 600°C with a 5°C/min ramping and held at this temperature for 2.5 hours for complete oxidation of the organic compounds. Then, with the same 5°C/min ramping, it is heated to 1000°C and held at this temperature for 5 hours.

Important Note:

If there is any amount of boron in the crystal structure, calcining at 1000°C will yield the SA_2 phase whereas calcination at 1100°C will form the S_4A_7 phase. If there is no boron at all, the calcination must be performed at 1100°C in order to produce the pure SA_2 phase.

Step 4:

This step is to improve the phase purity of the SA_2 powders. It is simply re-calcining the powders at 1000°C for 2 more times, performing grinding at the end of each calcination.

Step 5:

After calcination, the powder SA_2 needs to be calcined in a reducing atmosphere, which is 96 wt % N_2 and 4 wt % H_2.

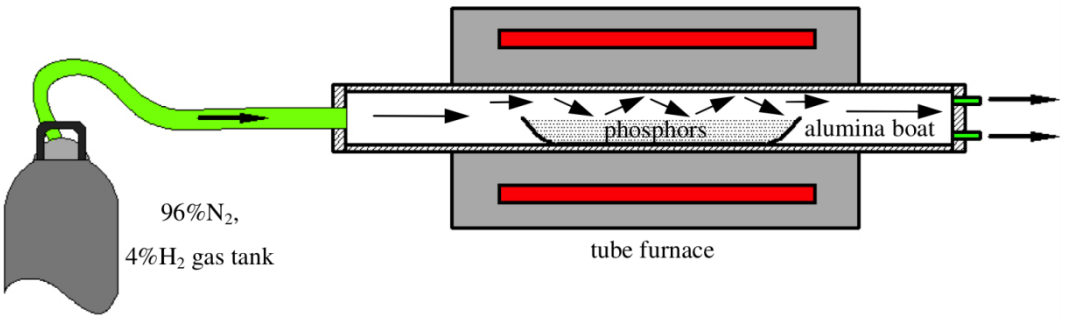

Figure 2.1 Schematic of the tube furnace used during the reduction process [13].

The SA_2 powders should be heated up to the same temperature as the calcination temperature with 5°C/min ramp and hold there for 3 hours. The furnace to be used is a tube

furnace as illustrated in Figure 2.1. The gas flow should be set to the maximum on the flowmeter.

However, for the SA_2 phase, this flow may require some adjusting according to the amount of gas left in the gas tank. Blackening of the powders was observed, when the gas flow through the furnace is too high. Even though this gray by-product phosphoresces, the brightness and the duration are not as high and long as that of properly reduced powders. The amount of this blackening increases as the B amount decreases. As a result, in case of such a problem, the reduction process should be repeated with the gas flow decreased.

At the end of a proper reduction process, SA_2 powders are slightly yellowish in color.

2.3 Characterization Tools

2.3.1 Transmission Electron Microscope (TEM)

Electron loss near edge spectroscopy (ELNES) and energy dispersive x-ray spectroscopy (EDX) measurements were performed in the VG STEM, a dedicated scanning transmission electron microscope (STEM) operated in UHV at an accelerating voltage of 100 kV in Stuttgart Center for Electron Microscopy, Max Planck Institute for Intelligent Systems (formerly Max Planck Institute for Metals Research), Stuttgart, Germany. The measurements were performed by Dr Vesna Srot. The convergence semi-angle was 10 mrad, and the collection semi-angle is 6.5 mrad. The time used to acquire B-*K* edge was 8 s, ×2.

2.3.2 X-Ray Diffraction (XRD)

X-ray diffraction measurements were performed using a Bruker AXS Advance D8 with a Cu-K_α source at Sabanci University, Istanbul.

2.3.3 Thermoluminescence (TL) Spectroscopy

Thermally stimulated emission spectroscopy measurements were performed in a Rexon UL-320 Series TLD Reader.

2.3.4 Photoluminescence (PL) Spectroscopy

Optical properties were characterized (photoluminescence and phosphorescence spectroscopy) using a HeCd laser (λ_{ex} = 325nm, KIMMON) and a fluorescence-specific spectrometer (Ocean Optics USB2000-FLG).

At this point, the author would like to share his experience on how to perform PL measurements with phosphorescent powders.

Figure 2.2 Lids of the eppendorf tubes are cut and filled with the SA_2 powder. Then the powder is pressed with the help of a magnetic stirrer.

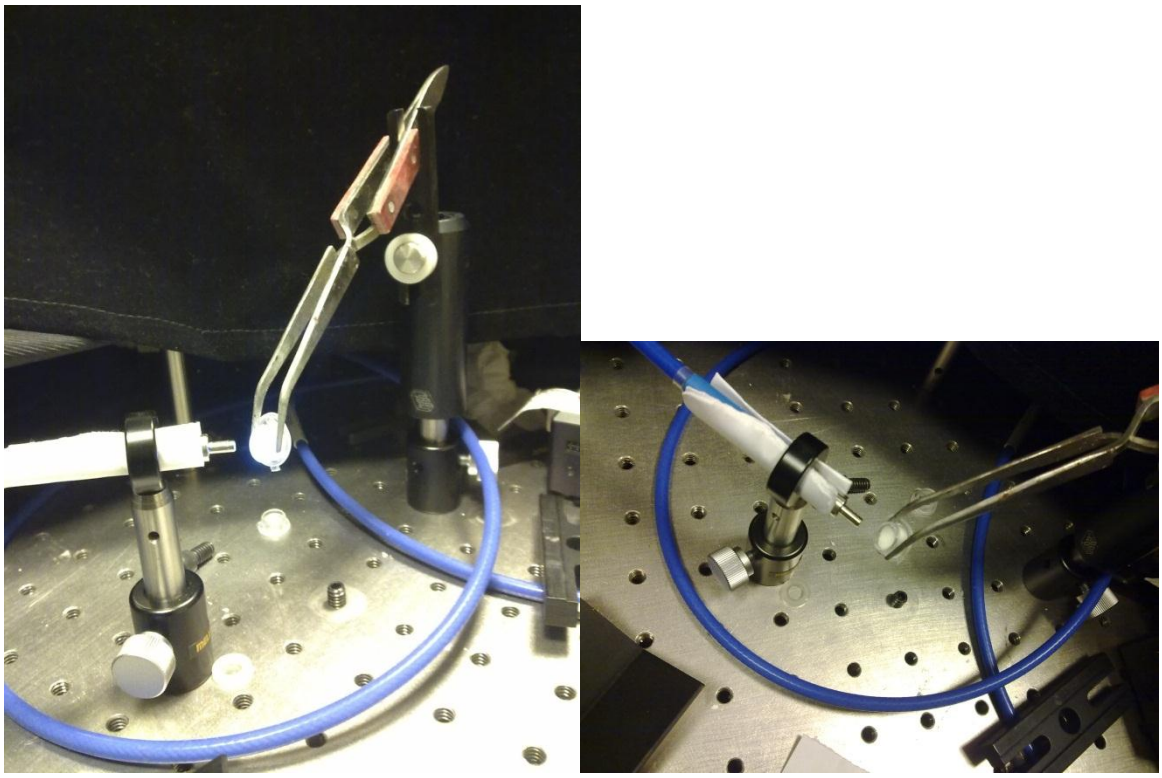

Figure 2.3 Using a reverse tweezer, the SA_2 loaded lids' position is fixed so that the laser is targeted directly to the center of the powder surface.

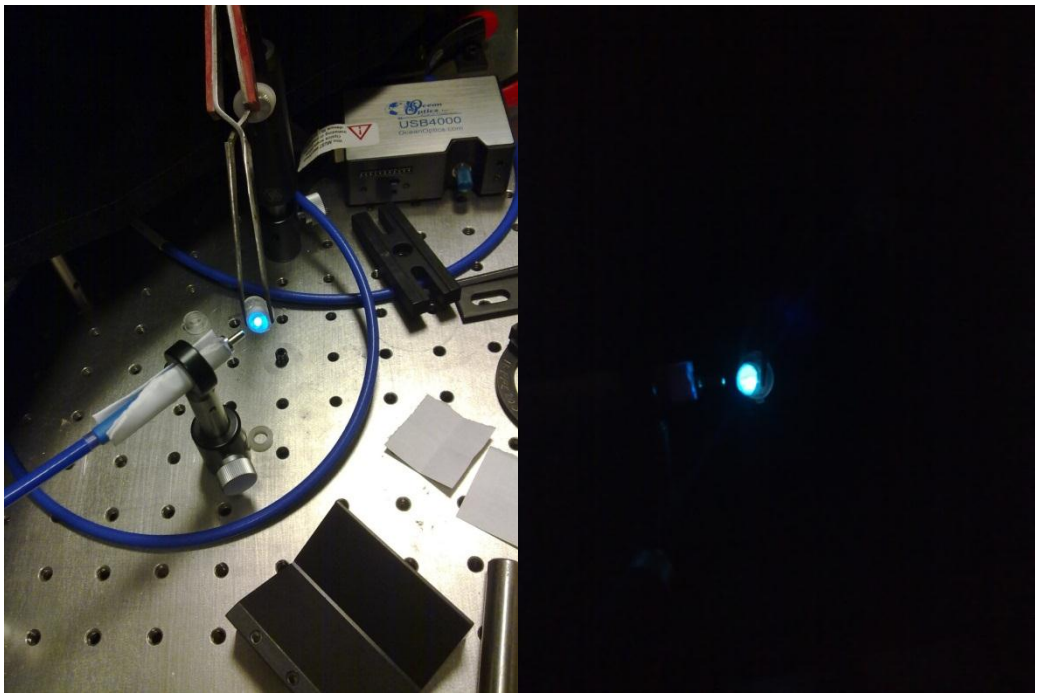

Figure 2.4 The powder surface is concave, so the detector collects emission from many directions leading to a high intensity.

CHAPTER 3. RESULTS

3.1 TEM Results

$SrAl_4O_7$ samples with 0, 10, 20 and 30 mol % B amounts are produced for ELNES studies. Since the VG STEM used for the spectra has also EDX capability, the EDX results were collected and will be presented when considered necessary.

Al-$L_{2,3}$ edges for $SrAl_4O_7$ with 0 mol % B

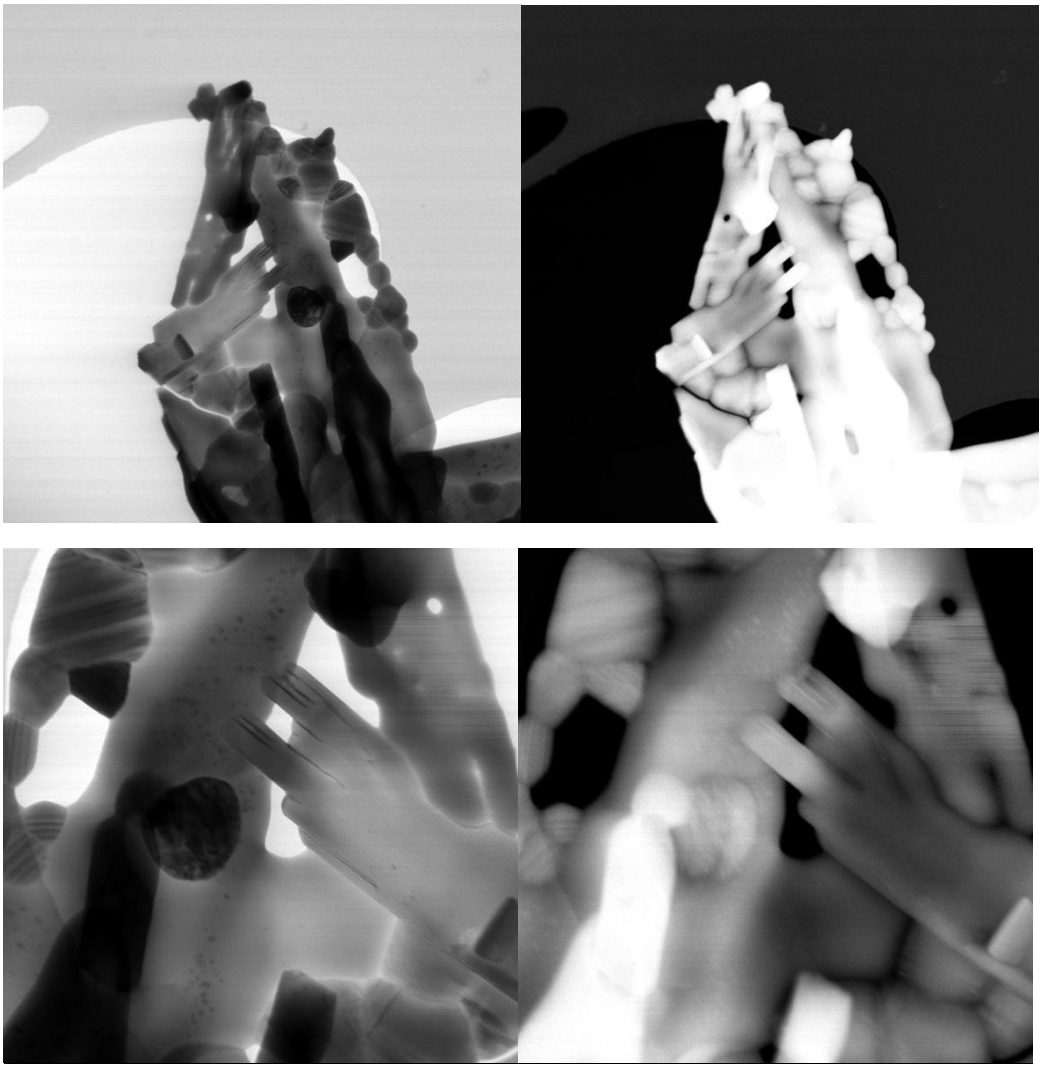

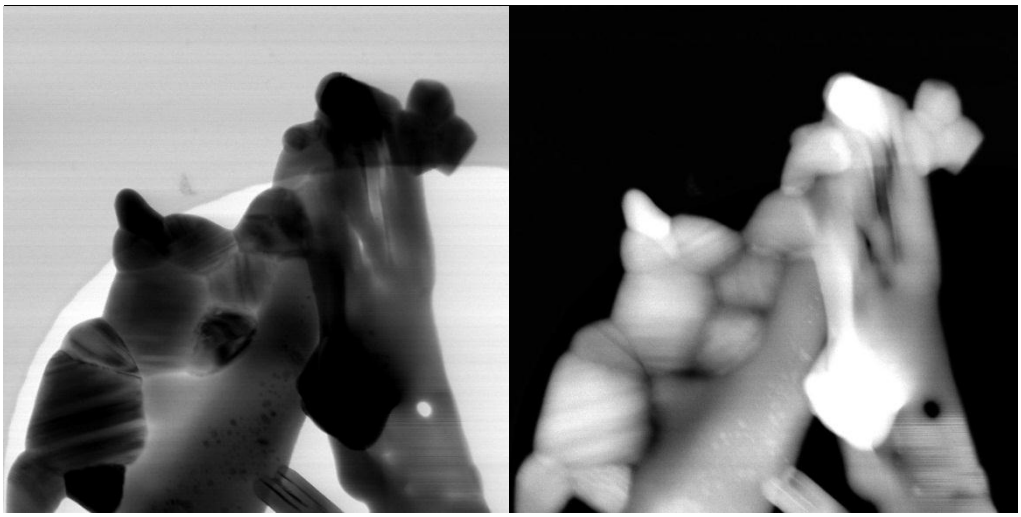

Figure 3.1 Bright field (images on the left) and dark field (images on the right) images of three different particles for $SrAl_4O_7$ with 0 mol % B.

Data was collected from 31 different locations. Three different type of Al-$L_{2,3}$ edges were observed.

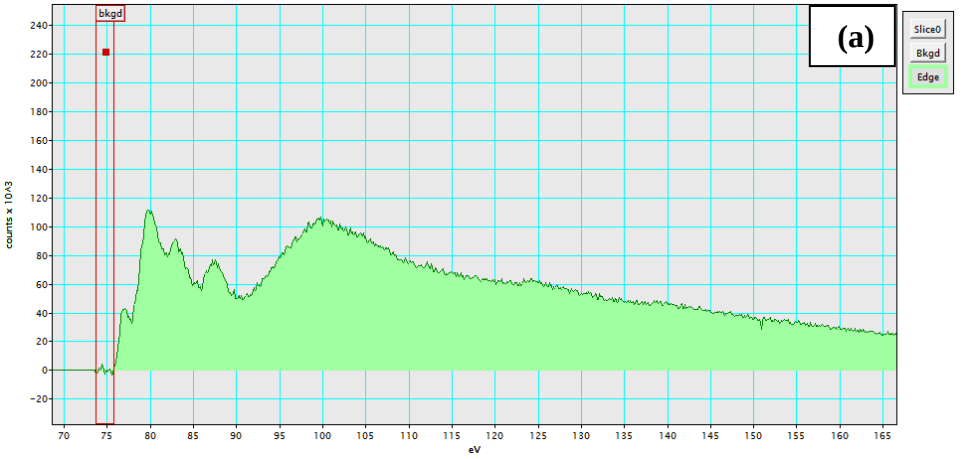
(a)
bkgd
Slice0
Bkgd
Edge
counts x 10^3
eV

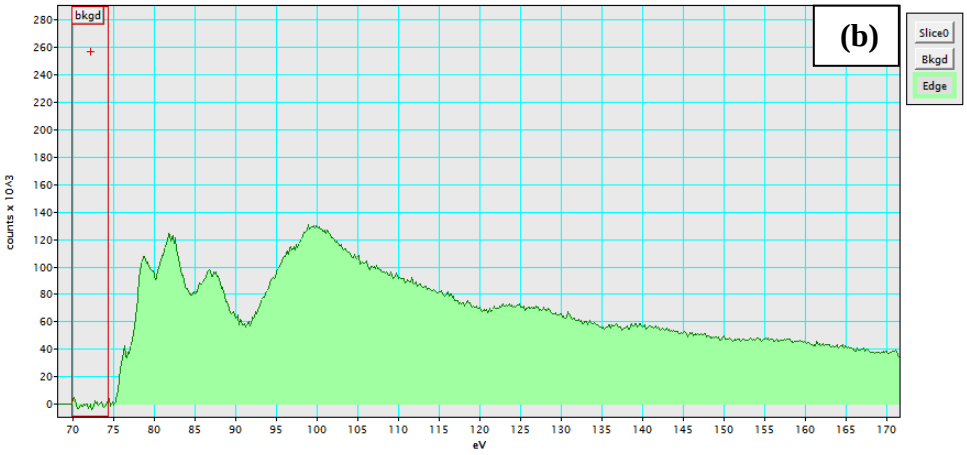
(b)
bkgd
Slice0
Bkgd
Edge
counts x 10^3
eV

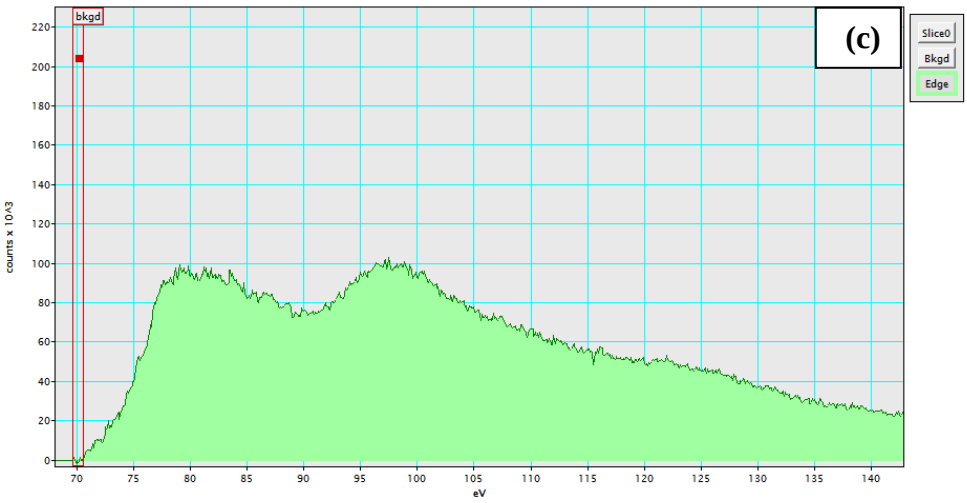
(c)
bkgd
Slice0
Bkgd
Edge
counts x 10^3
eV

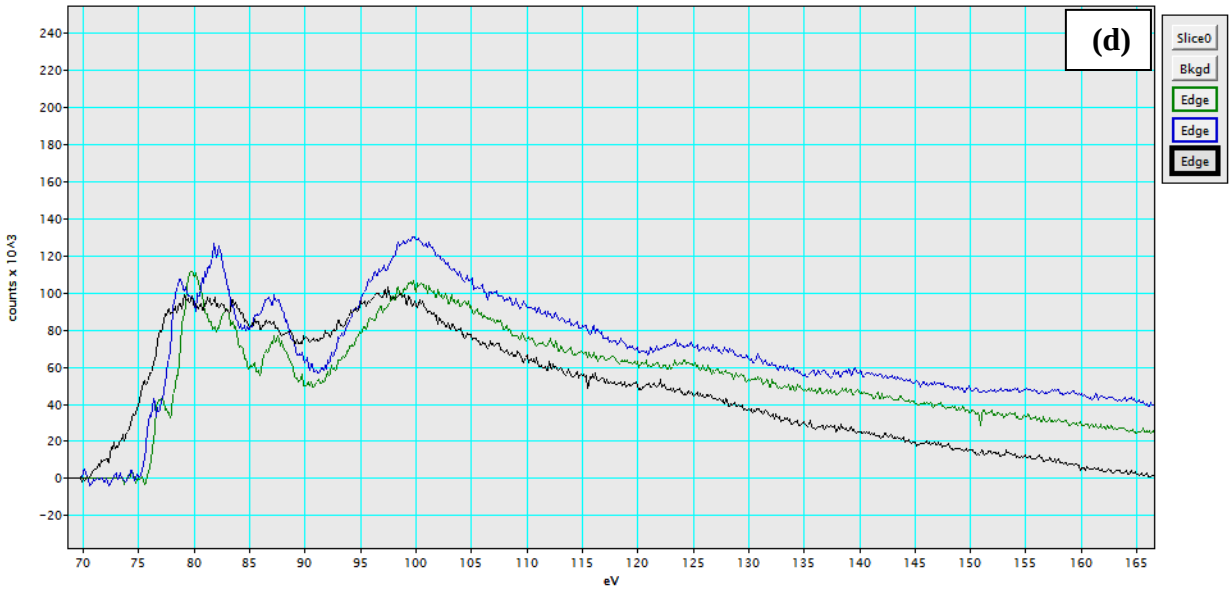

Figure 3.2 Three different Al-$L_{2,3}$ edges with Al/Sr ratio (according to the EDX data) (a) 4.76, (b) 2.42 and (c) 2.58. in (d) all three spectra are put together with green for the spectra in a, blue for the spectra in b and the black for the spectra in c.

Al-$L_{2,3}$ edges for $SrAl_4O_7$ with 10, 20 and 30 mol % B

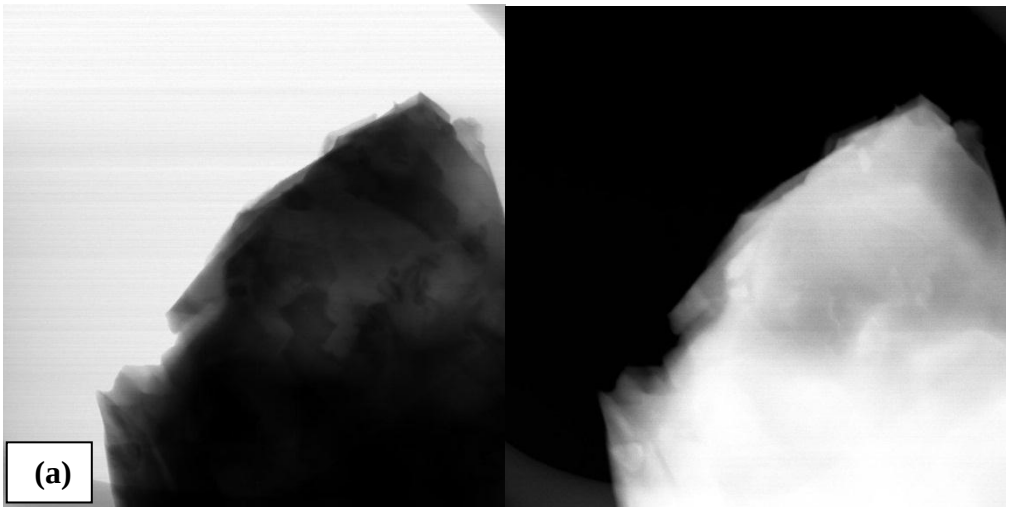

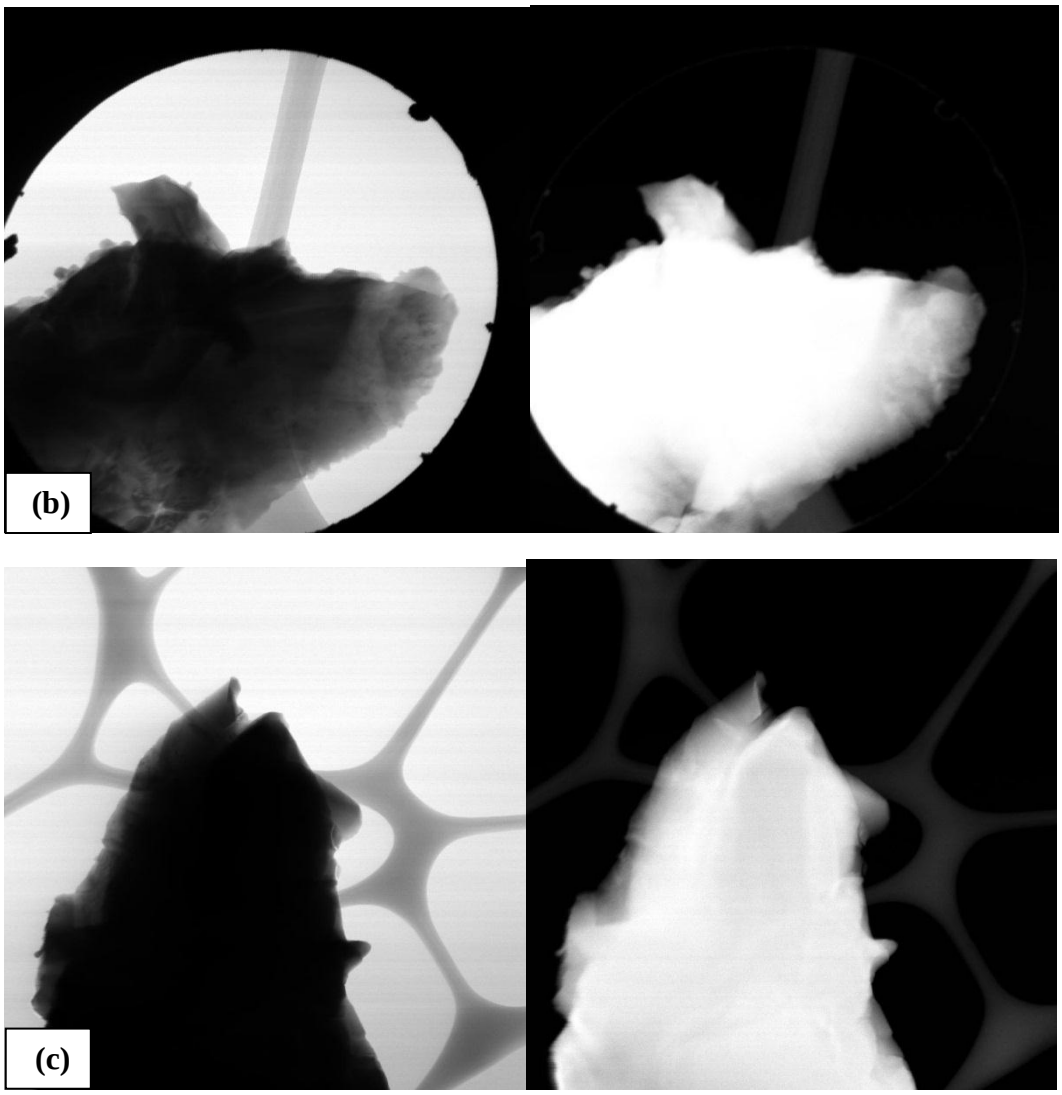

Figure 3.3 Bright field (images on the left) and dark field (images on the right) images of particles for $SrAl_4O_7$ with (a) 10 mol % B, (b) 20 mol % B (c) 30 mol % B.

Data was collected from at least 25 different locations and almost all of the points have one type of Al-$L_{2,3}$ edge.

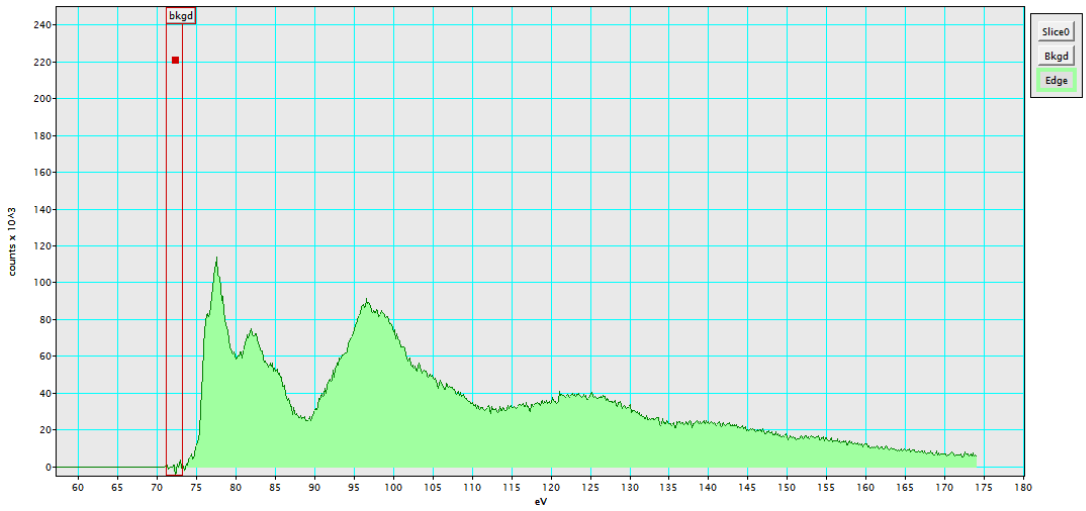

Figure 3.4 Al-$L_{2,3}$ edge observed for $SrAl_4O_7$ with 10, 20 and 30 mol % B.

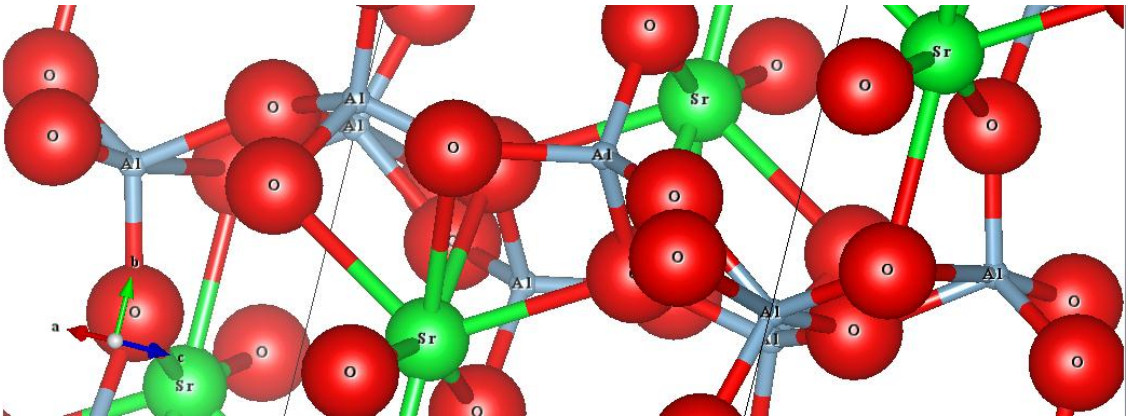

Figure 3.5 Crystal structure of SA_2 with the atoms labeled.

As seen from the Figure 3.2, SA_2 particles have 3 different Al-$L_{2,3}$ edges because in the crystal structure of SA_2 which was illustrated in Figure 3.5, Al atoms are both 4-fold and 5 fold coordinated. Since the ELNES spectra is sensitive to atomic positions and coordination, the observed three peaks come from 4-fold and 5-fold coordinated Al atoms and a linear combination of both, depending on the relative percentage of type of coordination [18].

B-*K* edges

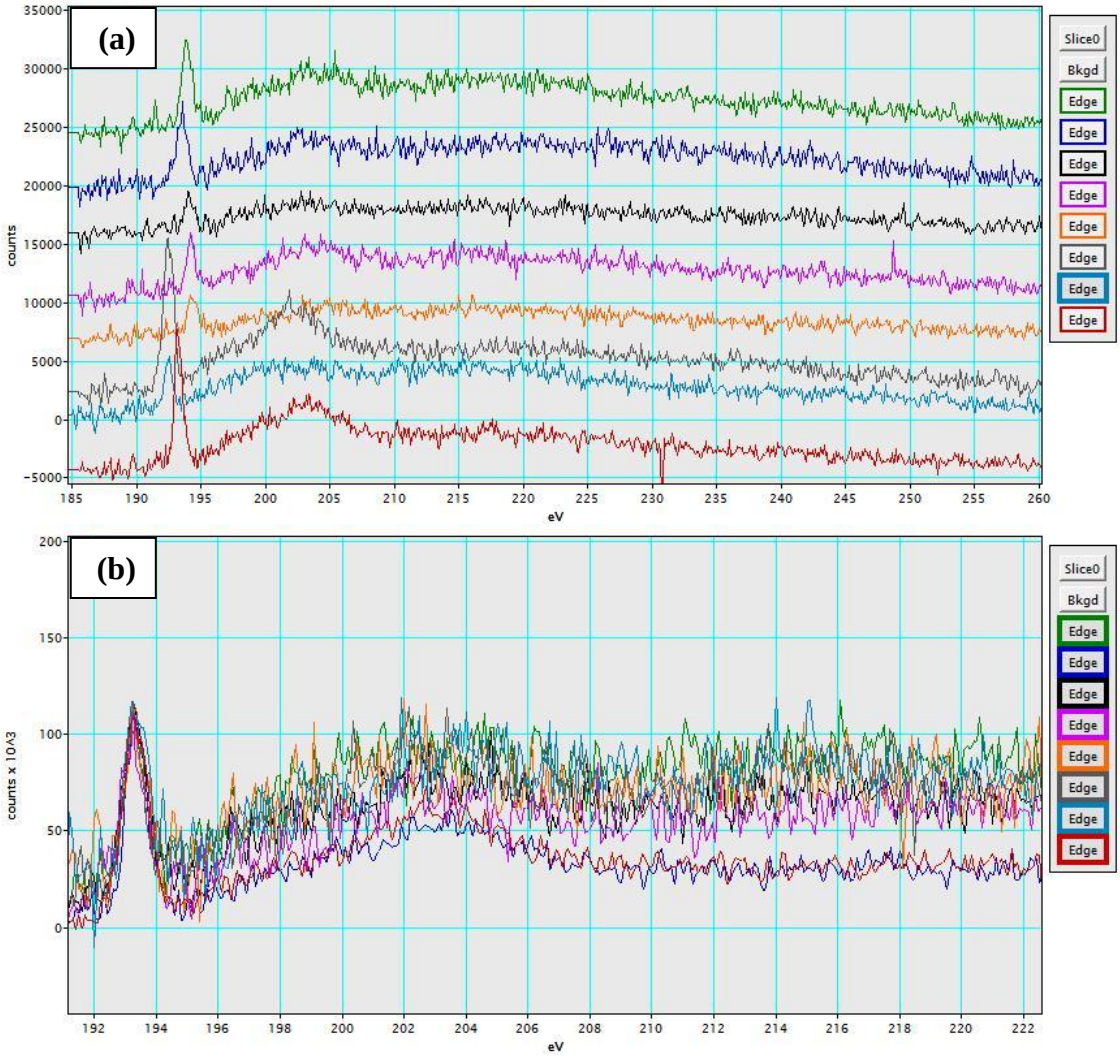

Figure 3.6 (a)B-*K* edges for 8 different locations on SA_2 powder with 10 mol % B. (b)All 8 spectra were aligned by their maximum.

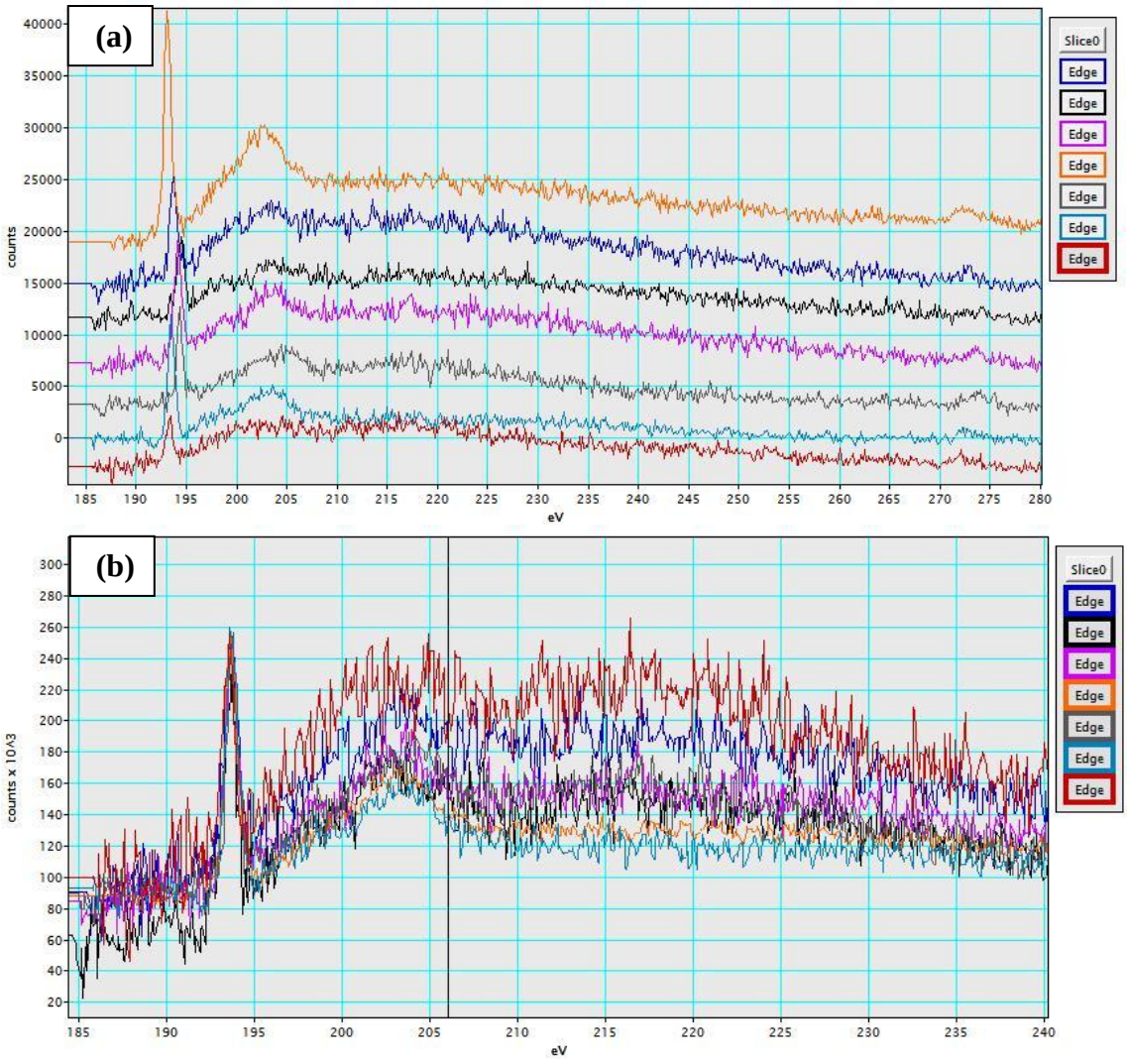

Figure 3.7 (a) B-*K* edges for 7 different locations on SA_2 powder with 20 mol % B. (b)All 7 spectra were aligned by their maximum.

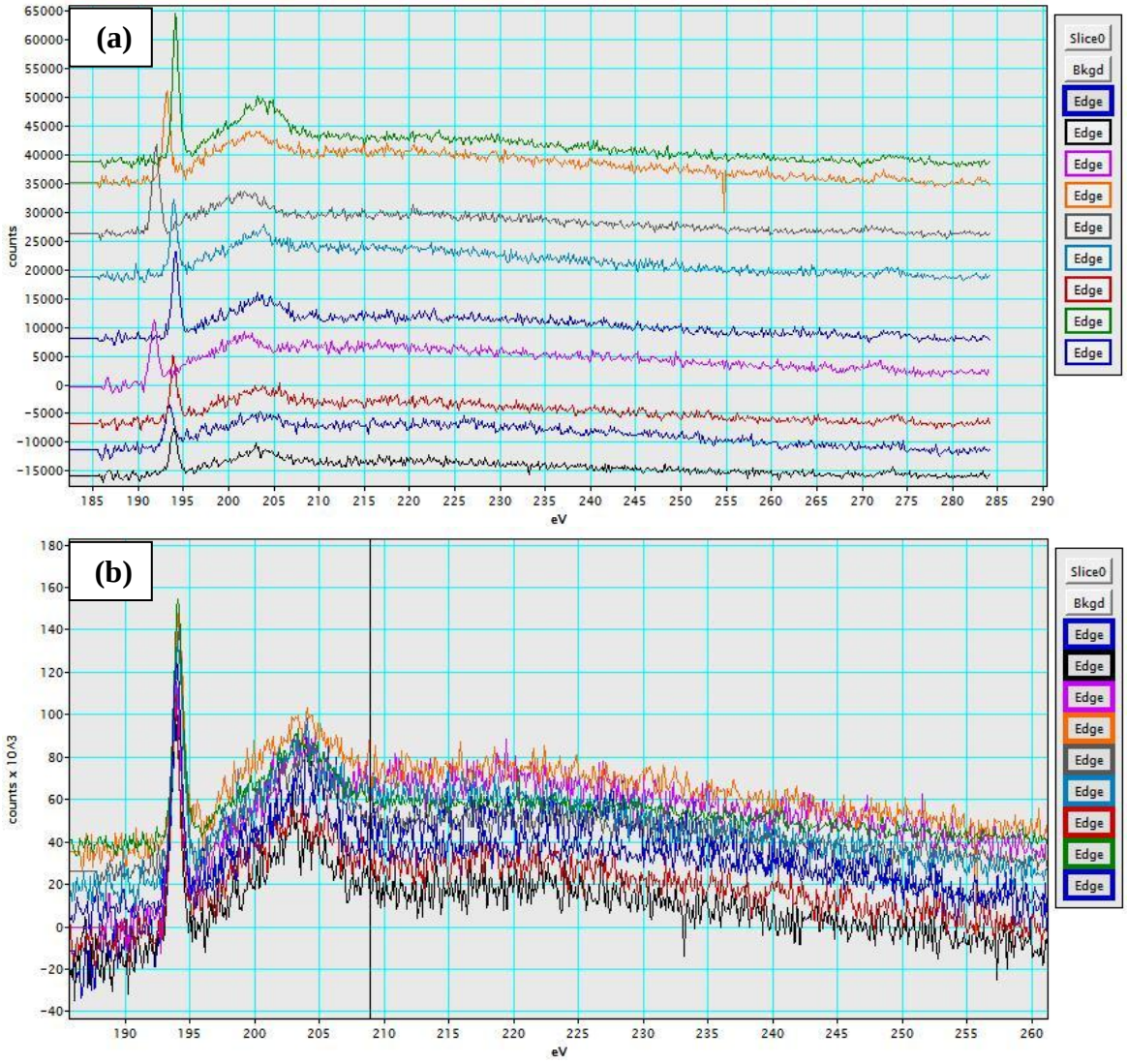

Figure 3.8 (a) B-*K* edges for 9 different locations on SA_2 powder with 30 mol % B. (b)All 9 spectra were aligned by their maximum.

As explained in the theory part, the first sharp peak caused by the π-antibonding corresponds to the trigonal character. In Figure 3.6*a*, the intensities of the first sharp peaks is relatively smaller and the second peak at about 202.5 eV which carries the tetragonal character is much broader compared to those of 20 amd 30 mol % B ones (Figures 3.7*a* and 3.8*a*). For the powders with 30 mol % B, this sharp peak has the highest intensity and the second broad peak is more like a triangle (Figure 3.8*a*). Therefore, there is such a transition as the boron amount increases.

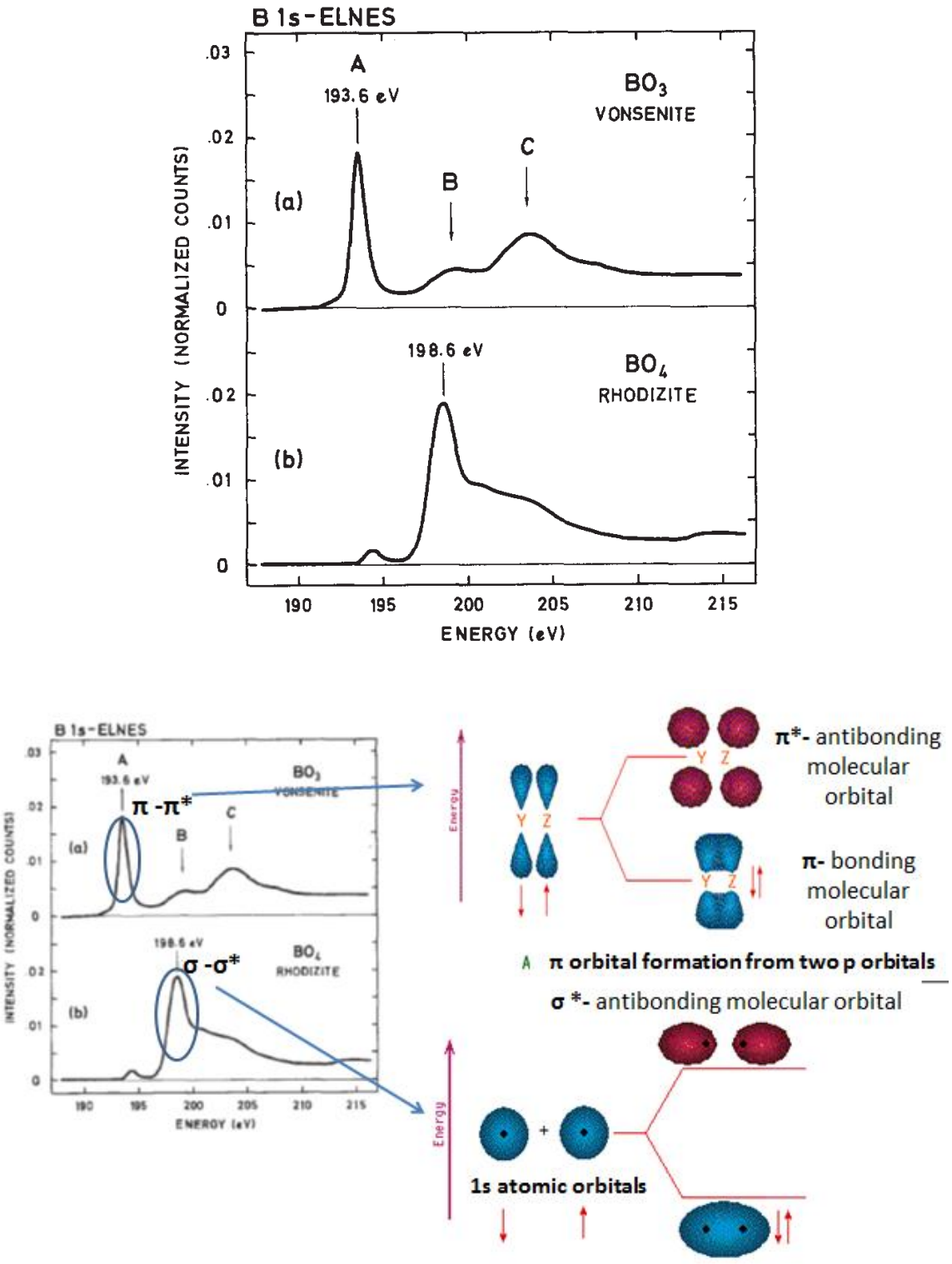

Figure 3.9 Boron 1s fingerprints measured from the minerals (a)vonsenite (planar-trigonal BO_3 coordination) and (b)rhodizite (tetrahedral BO_4 coordination) [14].

Electron energy loss spectroscopy (EELS) is a powerful tool for investigating local

bonding and coordination information, because the near edge structure is determined by subtle changes in bonding between nearest neighbor atoms. When this atom exists in different numbers and spatial arrangements in the crystal, the shape of the ELNES will show the characteristic differences that can be interpreted as the coordination fingerprints [15].

The pure 3-fold and 4-fold coordinated B-*K* edges were presented in the work of Sauer et al. [14] and shown in Figure 3.9.

When B is 3-fold coordinated, it has sp^2 hybridized orbitals. Overlapping of sp^2 hybrid orbitals give rise to π- π^* molecular orbitals. This first sharp peak in Figure 3.9 comes from π- π^* molecular orbitals. When B is 4-fold coordinated, it has sp^3 hybridized orbitals which form σ-σ^* molecular orbitals. Second broader peak in Figure 3.9 is a result of these molecular orbitals.

In the figures through 3.6 to 3.8, the observed B-K edges acquired from SA_2 powder samples always have a sharp high intensity peak around 193 eV and a broader one at around 203 eV suggesting that these ELNES fingerprints are those of a three-fold coordinated B. However, if the observation is performed more carefully, it will be clearer that the acquired ELNES fingerprints are missing two separate peaks (peak B and C in Figure 3.9).

It is also known that if the atom being investigated occurs in several coordinations in the crystal matrix, the near edge structure is a superposition of the corresponding ELNES fingerprints [14, 16, 17].

Due to the atomic size and charge of boron, it is possible for boron to substitute for an Al atom or go into the interstitial sites in the SA lattice. Al atoms can be found in different locations in SA_2, which has tetrahedral and pentahedral Al sites. To understand what happens to the B inside the crystal, a quantification of the ELNES data were performed.

3.1.1 Quantification of the Boron-K Edges

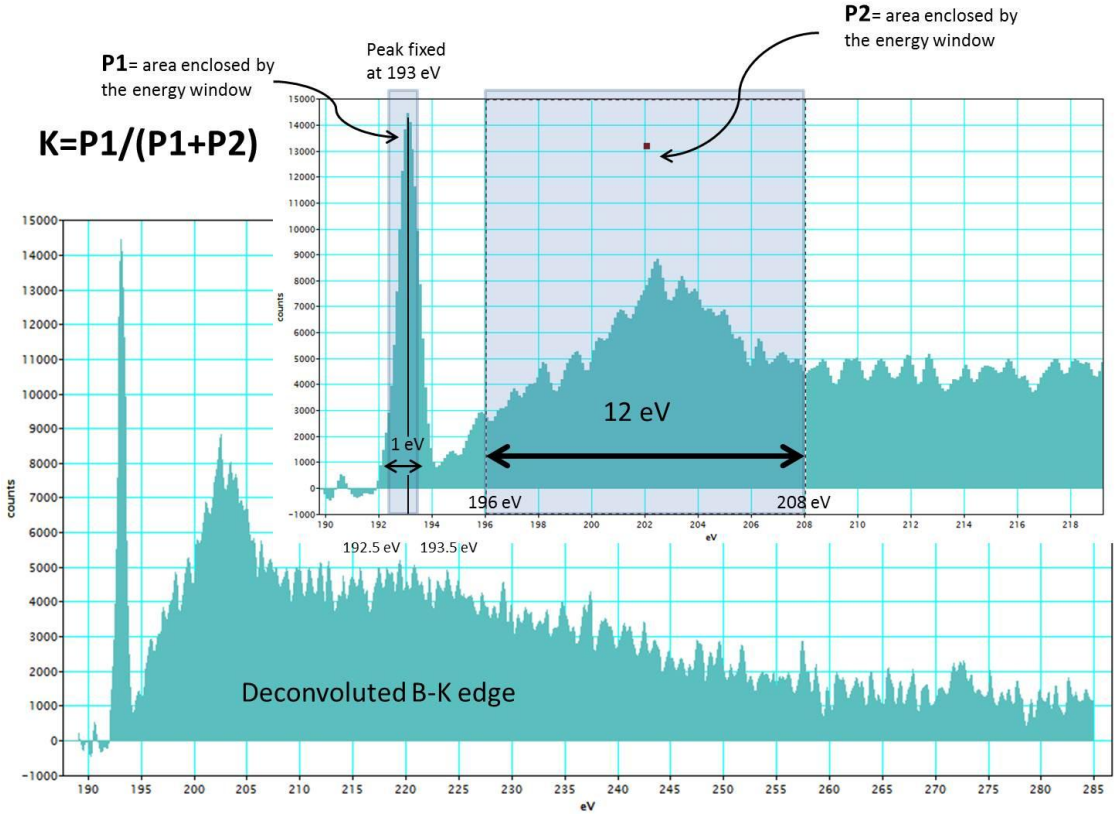

Figure 3.10 Deconvoluted B-*K* edge and determination of the integration window.

In order to eliminate multiple scattering effects, deconvolution was performed on the ELNES spectra, yielding the spectra in Figure 3.10. Prior to deconvolution, a single background subtraction was performed, as seen in Figure 3.11*a*. Because a better background fit might be achieved by using the two coupled regions of interest (ROI), the background removal was also performed using two coupled ROIs (Figure 3.11*b*). Both results will be presented for comparison.

In Figure 3.10, the sharp P1 peak at ~193 eV is the most distinctive peak for trigonally coordinated boron. Therefore, it is reasonable to conclude that the intensity of this P1 peak is directly proportional to the number of 3-fold coordinated boron atoms inside the crystal, and this relationship can be quantized by calculating the ratio of P1 to the entire signal,

which is P1 + P2. As a result, this K value ($K=P1/(P1+P2)$) is directly related to how much trigonal character exists in the location characterized.

The maxima of the P1 peak was set to 193 eV, and the positions and the widths of the integration windows are fixed for all spectra. For P1, the integration window starts at 192.5 eV and ends at 193 eV (1 eV wide). For P2, the window is set to fall between 196 eV and 208 eV (12 eV wide).

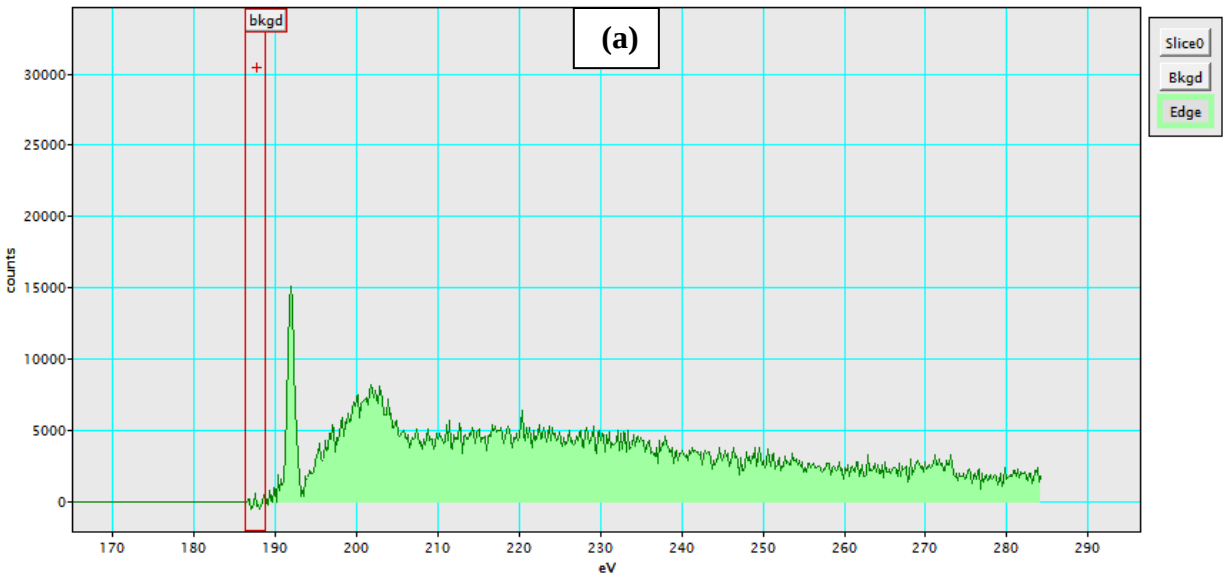

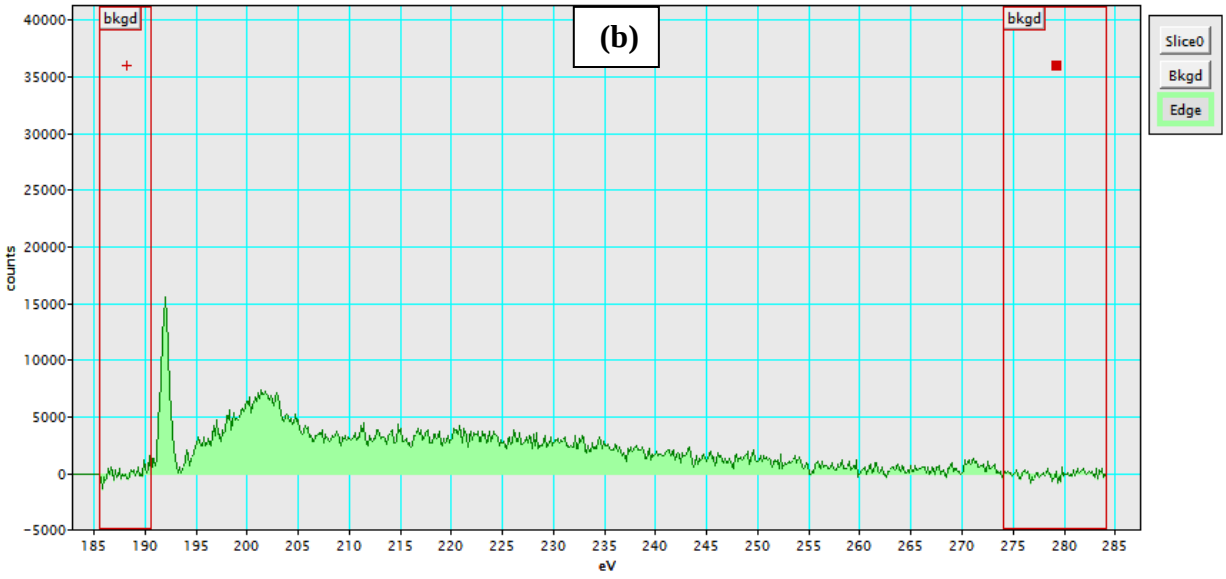

Figure 3.11 Background subtraction using a single ROI (*a*) and double ROIs (*b*).

As mentioned before, EDX data was also recorded for all the points, from which ELNES spectra was collected. It was observed that, whenever the P1 peak has a higher intensity, the atomic ratio Al/Sr decreases. We called this Al/Sr ratio M and evaluated for a correlation between K(*P1/(P1+P2)*) vs M.

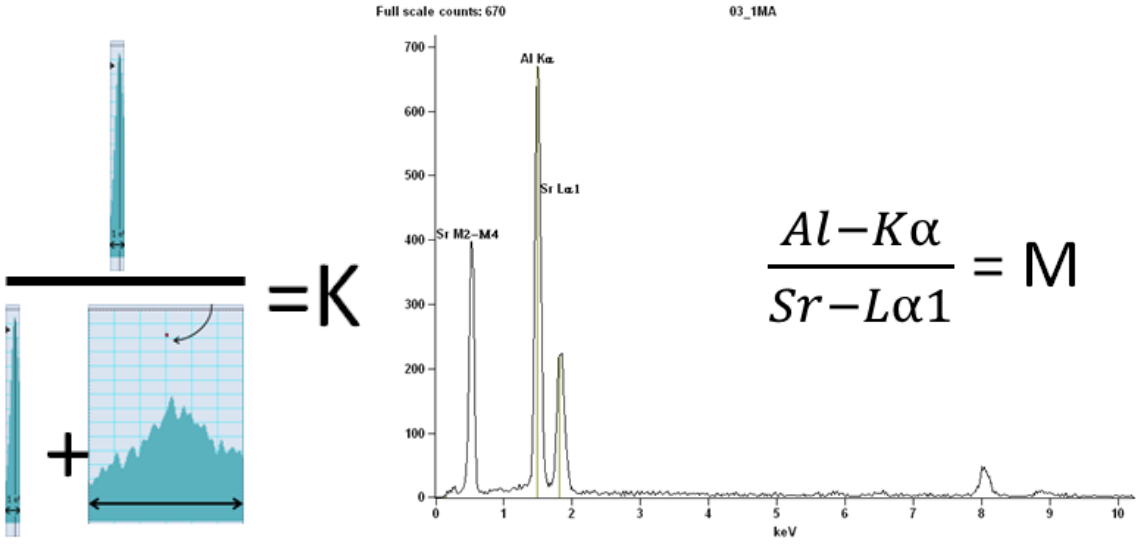

Figure 3.12 Definition of the parameters K and M.

The error calculations are necessary for both K and M. The error in K is calculated as follows:

$$\Delta\left(\frac{P_1}{P_1+P_2}\right)=\Delta K=\left(\frac{\partial K}{\partial P_1}\right)\partial P_1+\left(\frac{\partial K}{\partial P_2}\right)\partial P_2 \quad =\left(\frac{1}{P_1+P_2}-\frac{P_1}{\left(P_1+P_2\right)^2}\right).\Delta P_1+\left(\frac{P_1}{\left(P_1+P_2\right)^2}\right).\Delta P_2$$

Whereas $P_1=\sqrt{I\left(P_1\right)}$ and $P_2=\sqrt{I\left(P_2\right)}$.

The error in M is calculated as follows:

$$\Delta\left(\frac{Al}{Sr}\right)=\Delta M=\left(\frac{\partial M}{\partial Al}\right)\Delta Al+\left(\frac{\partial M}{\partial Sr}\right)\Delta Sr \quad =\Delta M=\frac{\Delta Al}{Sr}+\frac{Al}{Sr^2}\Delta Sr$$

Atom % errors are given by the software. So, all that is needed is to put the values in the equations.

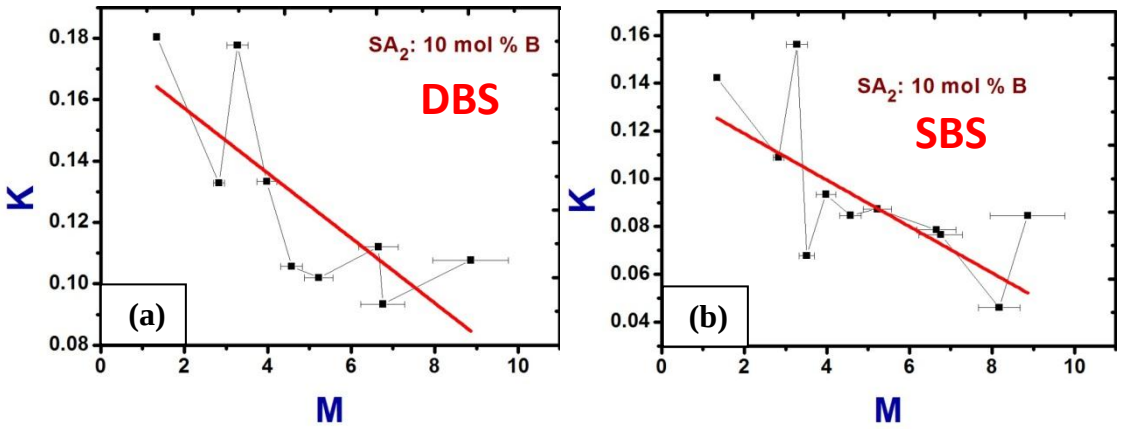

Figure 3.13 K vs M plot for SA_2 with 10 mol% B after (a)double background subtraction (DBS) and (b)single background subtraction (SBS).

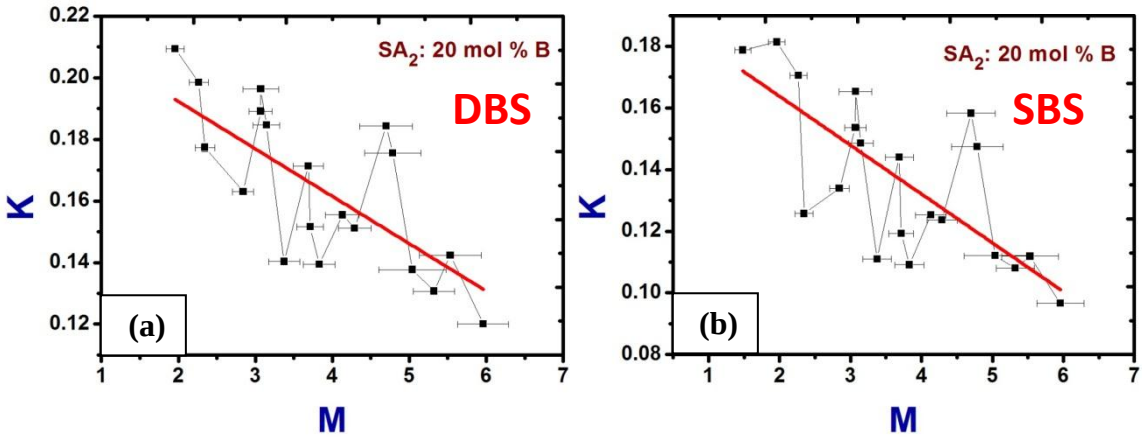

Figure 3.14 K vs M plot for SA_2 with 20 mol % B after (a)double background subtraction (DBS) and (b)single background subtraction (SBS).

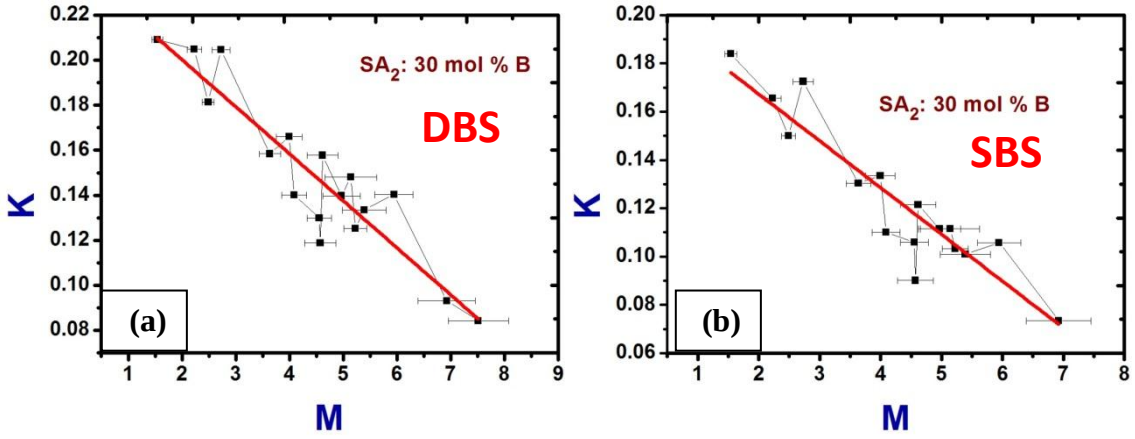

Figure 3.15 K vs M plot for SA_2 with 30 mol % B after (a)double background subtraction (DBS) and (b)single background subtraction (SBS).

Figures 3.13, 3.14 and 3.15 suggests that as the boron going into the lattice has more trigonal character, the number of Al atoms decreases, assuming that the number of Sr atoms is fixed. As a result, TEM studies lead to the following conclusions:

- A qualitative analysis of ELNES results (ELNES fingerprinting) revealed that boron incorporated into the SA_2 lattice occurs mostly in trigonal coordination.

- The correlation of the B-K edge quantification analysis to the EDX composition analysis confirms that the trigonally coordinated boron might occur as a result of Al-site substitution.

3.2 XRD Results

This part of the characterization was performed on both $SrAl_4O_7$ (SA_2) and $Sr_4Al_{14}O_{25}$ (S_4A_7) powders doped with varying amounts of boron.

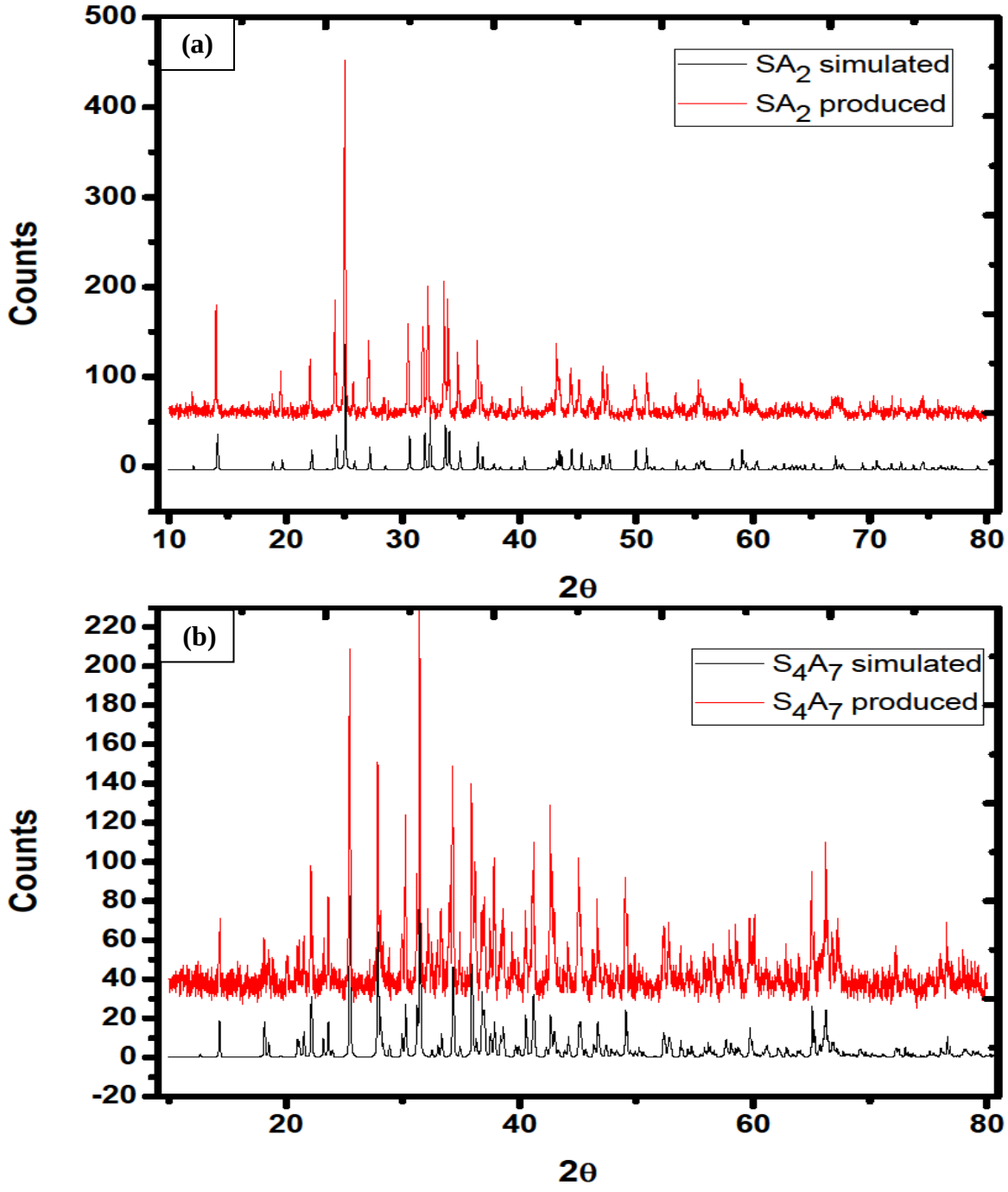

Figure 3.16 Confirmation of phase purity of SA_2 and S_4A_7 powders produced. XRD spectra for (a) SA_2 produced vs simulated and (b) S_4A_7 produced vs simulated.

Figure 3.16 shows how well the XRD spectra of produced powders fit to those simulated. Therefore, the modified Pechini method used is a successful technique for maintaining phase purity. By processing the powders via solution polymerization, boron can be

incorporated up to 30 mol %, while still maintaining the phase purity for both SA_2 and S_4A_7 phases. The corresponding crystal structures are presented below (Figure 3.17):

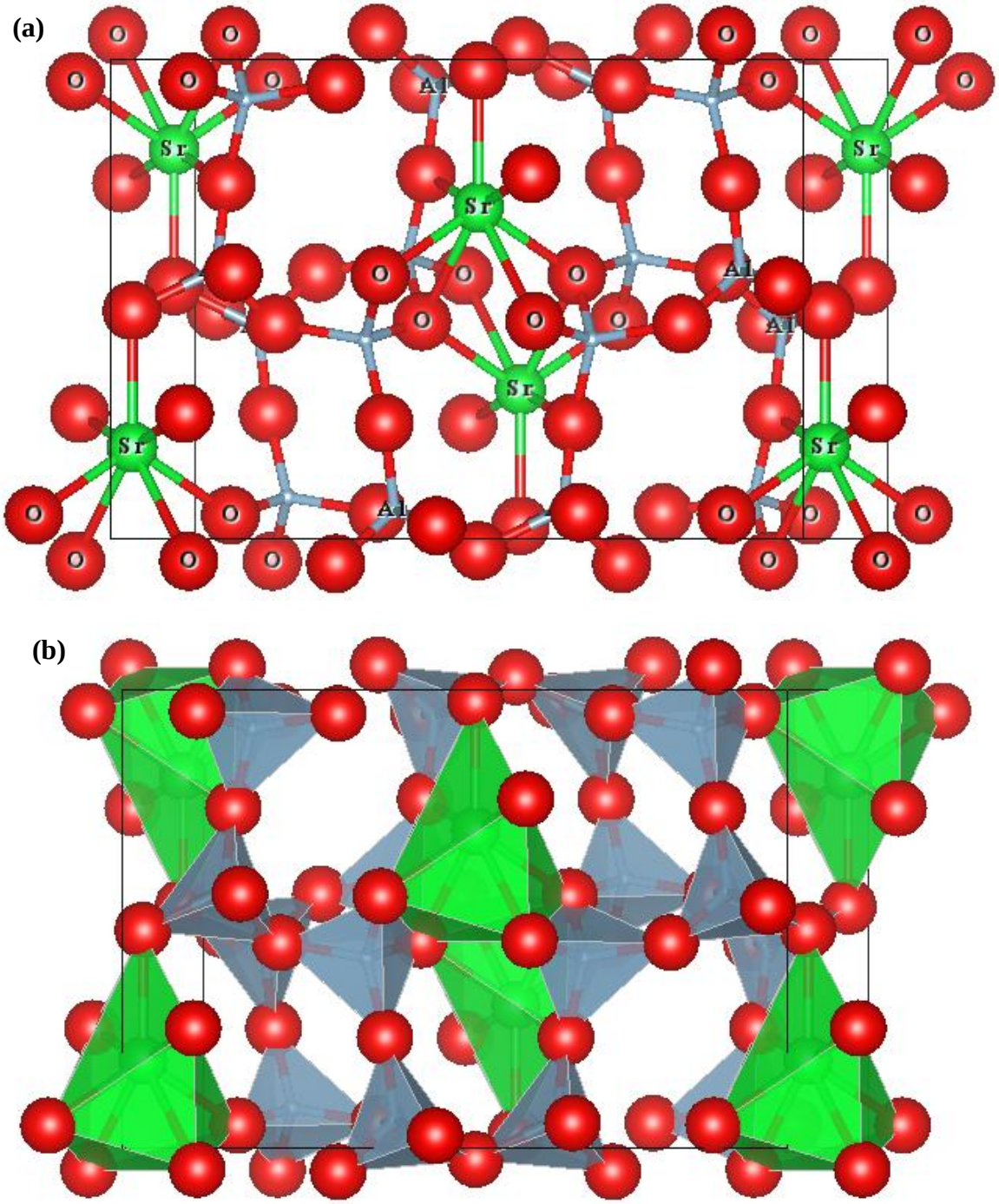

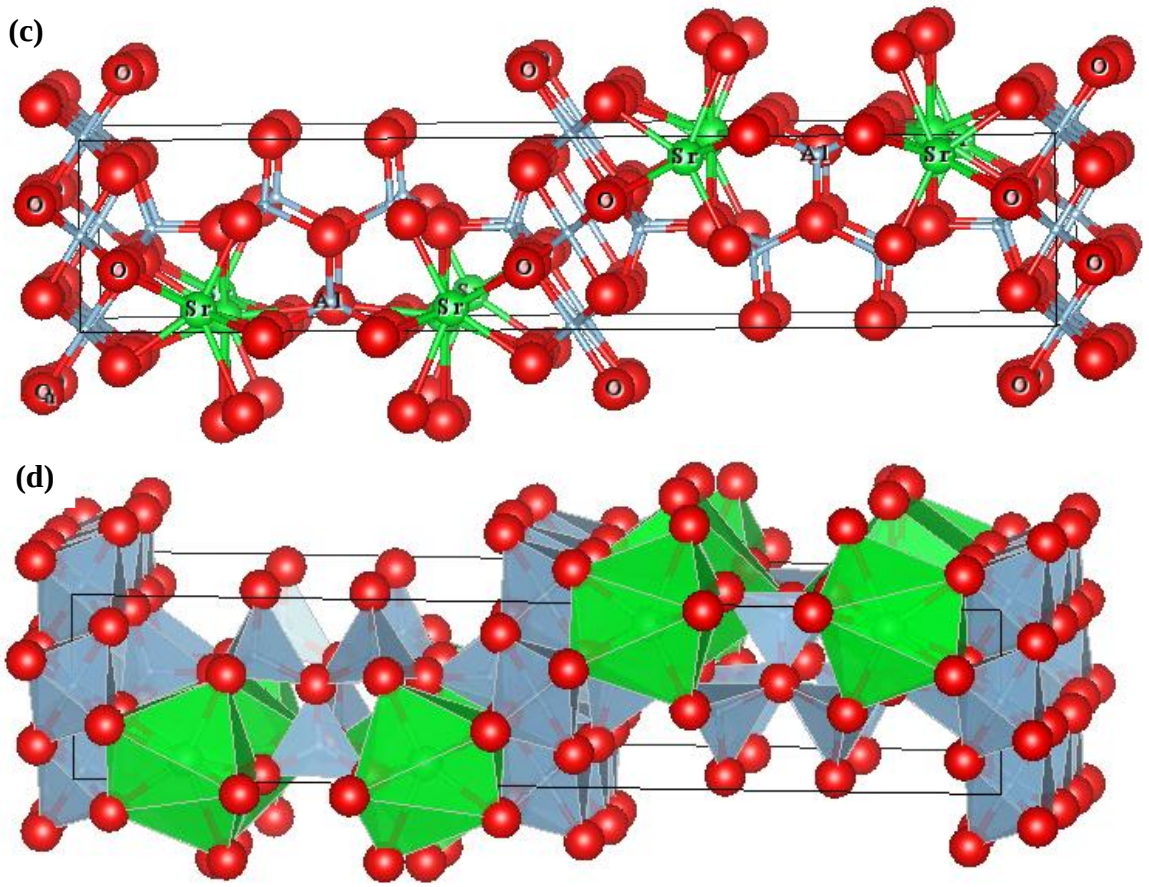

Figure 3.17 SA_2crystal in (a) ball and stick model (b) polyhedra and S_4A_7 crystal in (c) ball and stick model (d) polyhedra. Sr: green, O: red and Al: blue [Vesta software].

The SA_2 crystal has 4-fold and 5-fold coordinated Al sites, and the S_4A_7 crystal has 4-fold and 6-fold coordinated Al sites. Both structures have large vacant positions considering the very small size of B atom. Therefore, B can easily go into interstitials as well as substitute an Al atom.

3.2.1 Investigating the effect of B in crystal structure via determining the Peak Shifts

In order to understand the effect of boron to the crystal lattice, a peak shift study was conducted. The first idea was to compare the positions of the maximum diffracted intensity peaks of each phase, which is the -311 crystallographic planes for SA_2 and the 421 crystallographic planes for S_4A_7. However, the degree of shift does fall within the built-in

mechanical error in the instrument, rendering the shifts in peak positions were impossible to detect.

As a solution to this problem, a reference spectrum was needed. The maximum intensity peaks of SA_2 and S_4A_7 are both at around 25° and that of graphite is located at around 26.5°, which makes it a perfect candidate to be employ as such a reference. This process was performed only for SA_2 phase.

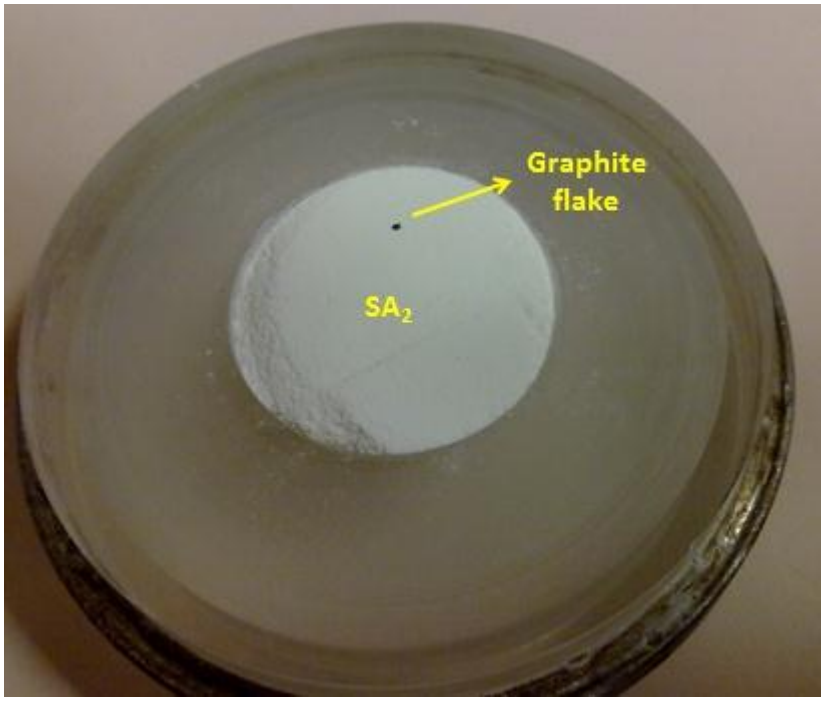

Figure 3.18 XRD sample holder loaded with SA_2 powder and a single graphite flake.

The determination of the peak positions were performed via calculating the center of gravities in the software EVA (Figure 3.19).

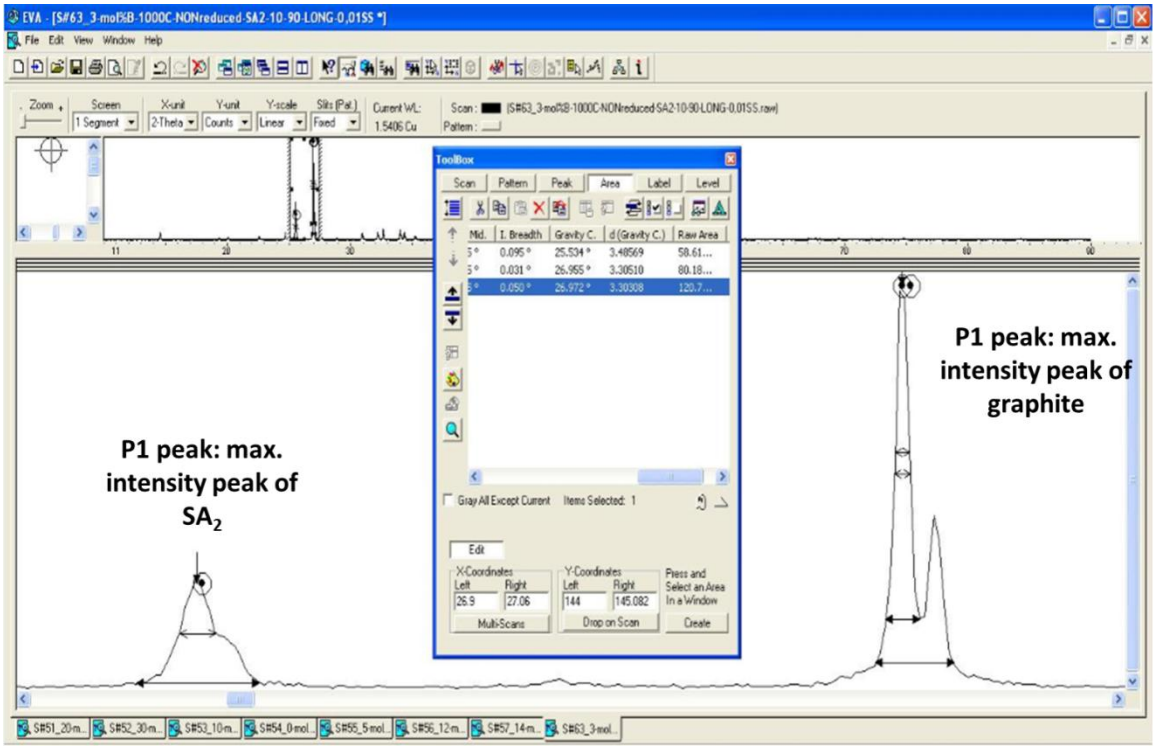

Figure 3.19 Calculating the center of gravities for SA_2 and graphite peaks via EVA, the spectral analysis software.

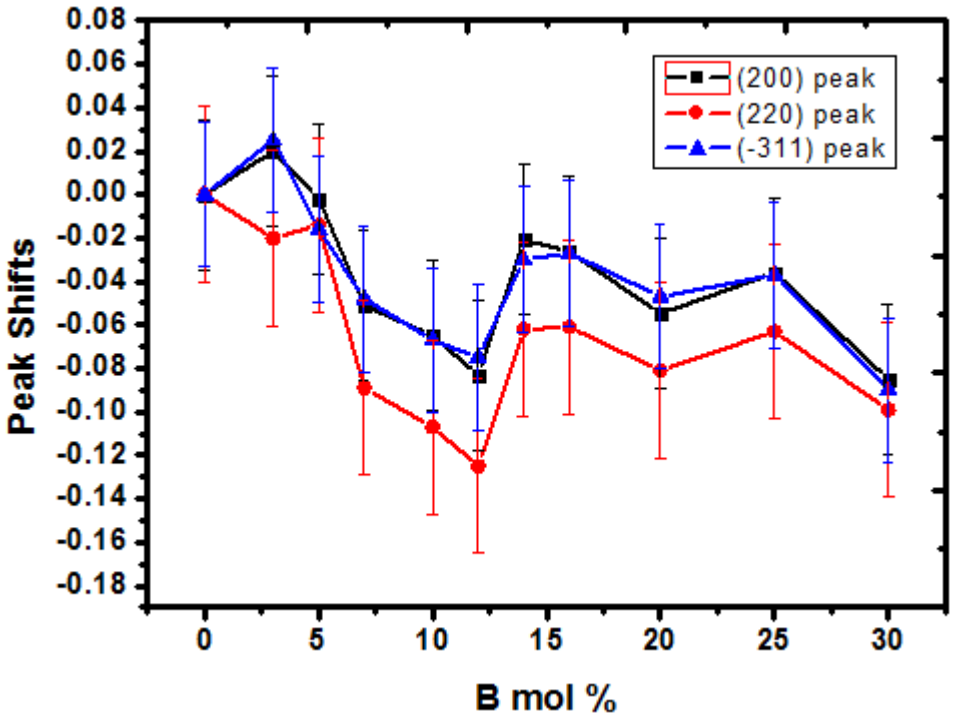

Figure 3.20 Peak shifts in varying amounts of B doped SA_2 with respect to the SA_2 with no boron. Black, red and blue are for the shifts in (200), (220) and (-311) peaks respectively.

From Figure 3.20, no conclusive discussion can be made. The peak shifts seem to follow no specific pattern. The whole patter falls within the error bars.

3.2.2 Effects of Intermediate Grinding on SA_2 powders

Powders were grounded and then calcined for a total of 3 times to see if this intermediate grinding helps to improve the phase purity of SA_2 powders.

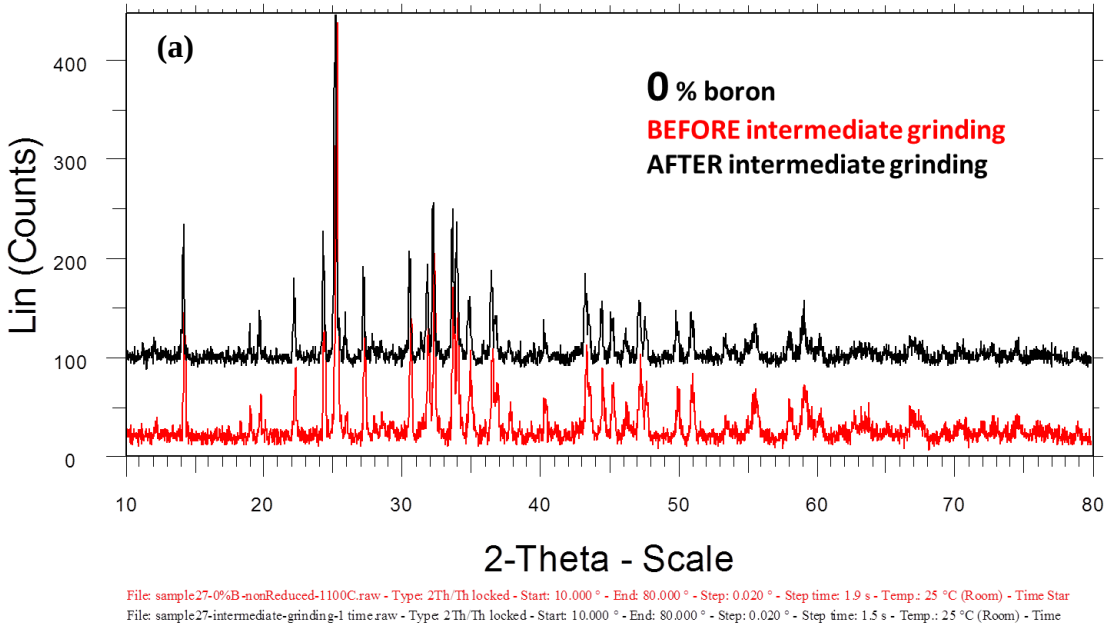

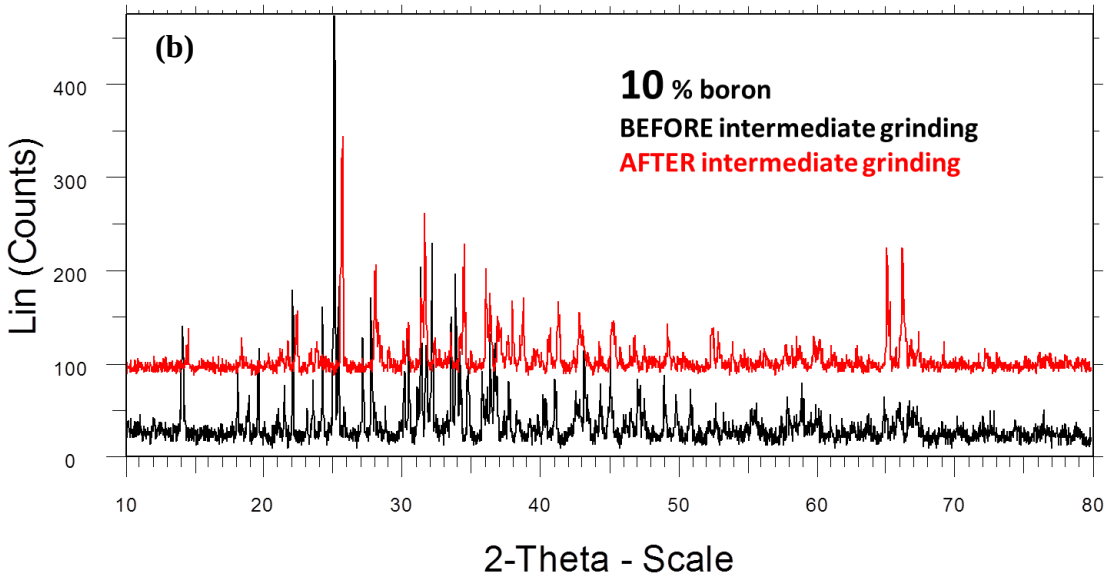

File: sample28-10%B-nonReduced-1100C.raw - Type: 2Th/Th locked - Start: 10.000 ° - End: 80.000 ° - Step: 0.020 ° - Step time: 1.9 s - Temp.: 25 °C (Room) - Time St
File: sample28_-_afterRECALC-10%B-nonReduced-1100C.raw - Type: 2Th/Th locked - Start: 10.000 ° - End: 80.000 ° - Step: 0.020 ° - Step time: 1.5 s - Temp.: 25 °C (

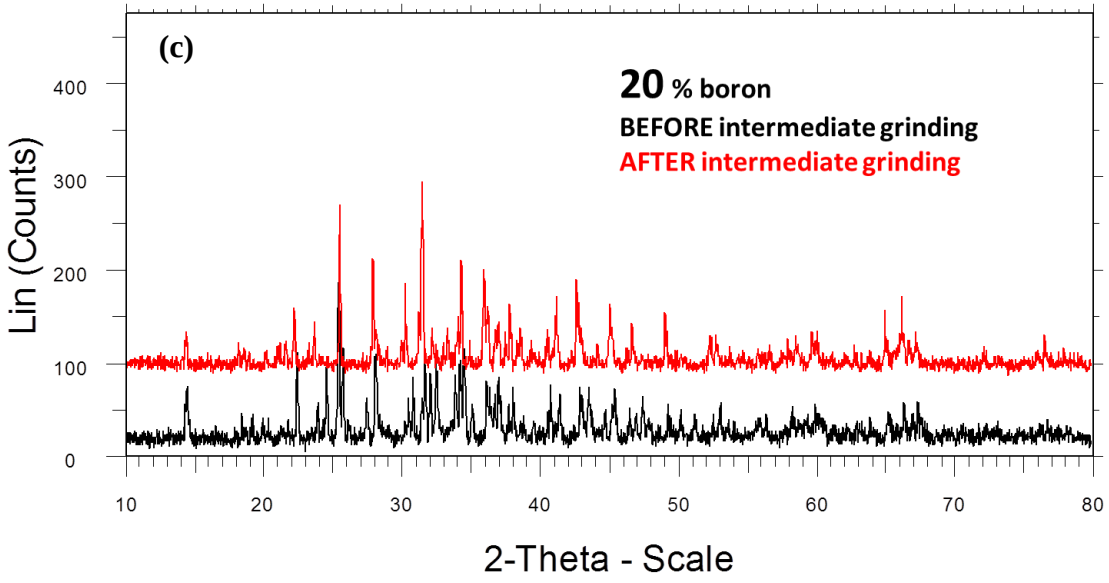

File: sample29-20%B-nonReduced-1100C.raw - Type: 2Th/Th locked - Start: 10.000 ° - End: 80.000 ° - Step: 0.020 ° - Step time: 2. s - Temp.: 25 °C (Room) - Time Started: 14 s - 2
File: sample29_-_afterRECALC-10%B-nonReduced-1100C.raw - Type: 2Th/Th locked - Start: 10.000 ° - End: 80.000 ° - Step: 0.020 ° - Step time: 1.5 s - Temp.: 25 °C (Room) - Tim

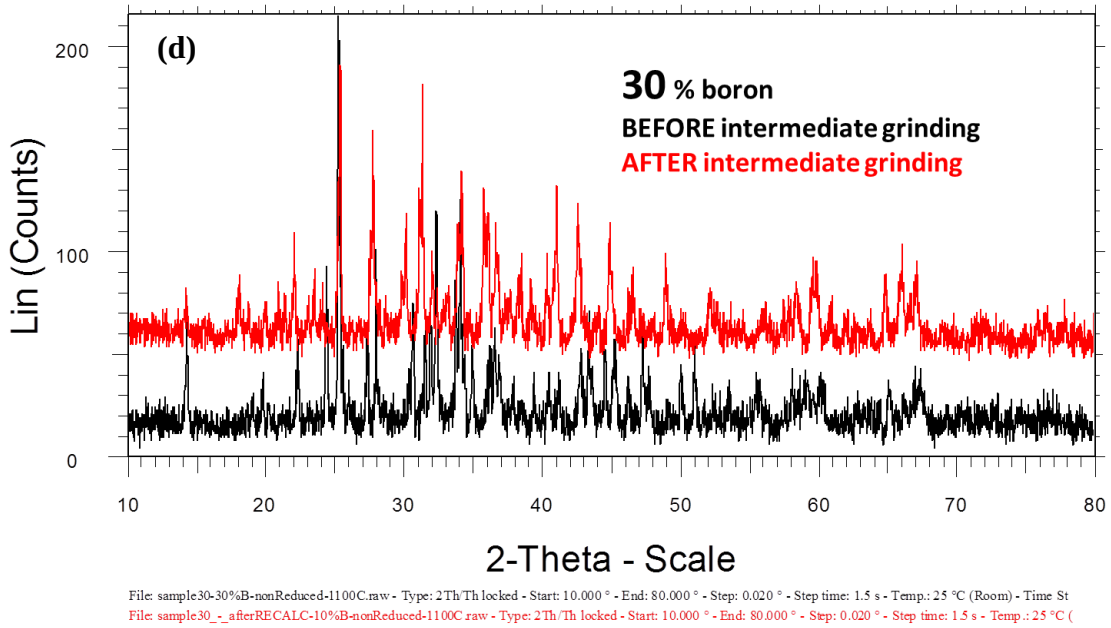

Figure 3.21 The XRD spectra before and after intermediate grinding for SA_2 powders with (a) 0 mol% B, (b) 10 mol% B, (c) 20 mol% B and (d) 30 mol% B. (All the red spectra are those which are after intermediate grinding except the one shown in part *a*, in which the black spectrum is the one after intermediate grinding).

Figure 3.21 shows the effect of intermediate grinding, which is eliminating some of the peaks and sharpening other ones. The SA_2 powders with 30 mol% B are important to note as this spectrum shows a poor signal-to-noise ratio.

3.2.3 Effects of Calcination Temperature on Crystal Structure

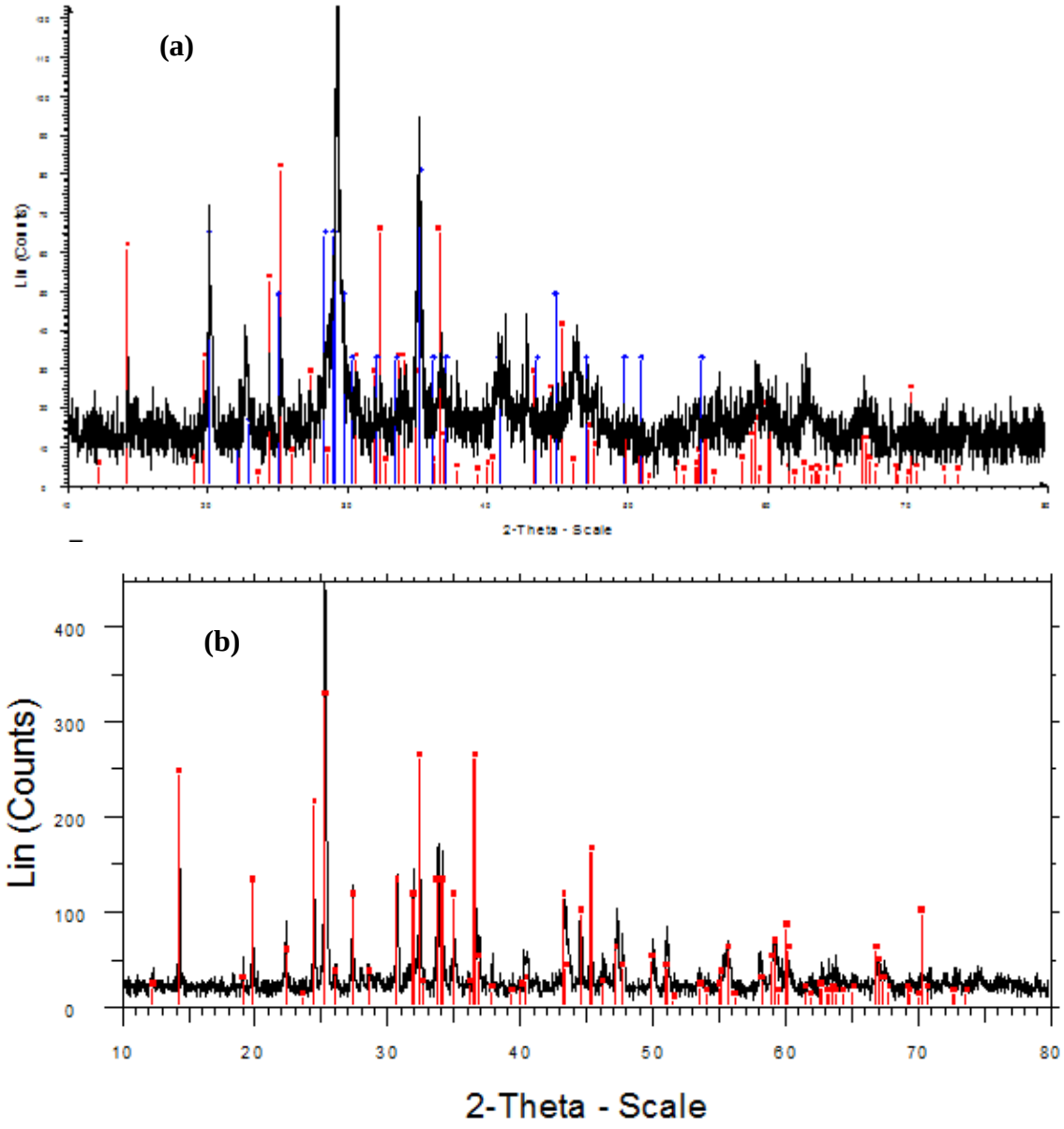

Figure 3.22 The XRD spectra for SA_2 powders with 0 mol% B calcined at (*a*) 1000°C and (b) 1100°C. Red peak labels: $SrAl_4O_7$ (SA_2) and blue ones: $SrAl_4O_7$ but a different phase, not the usual SA_2.

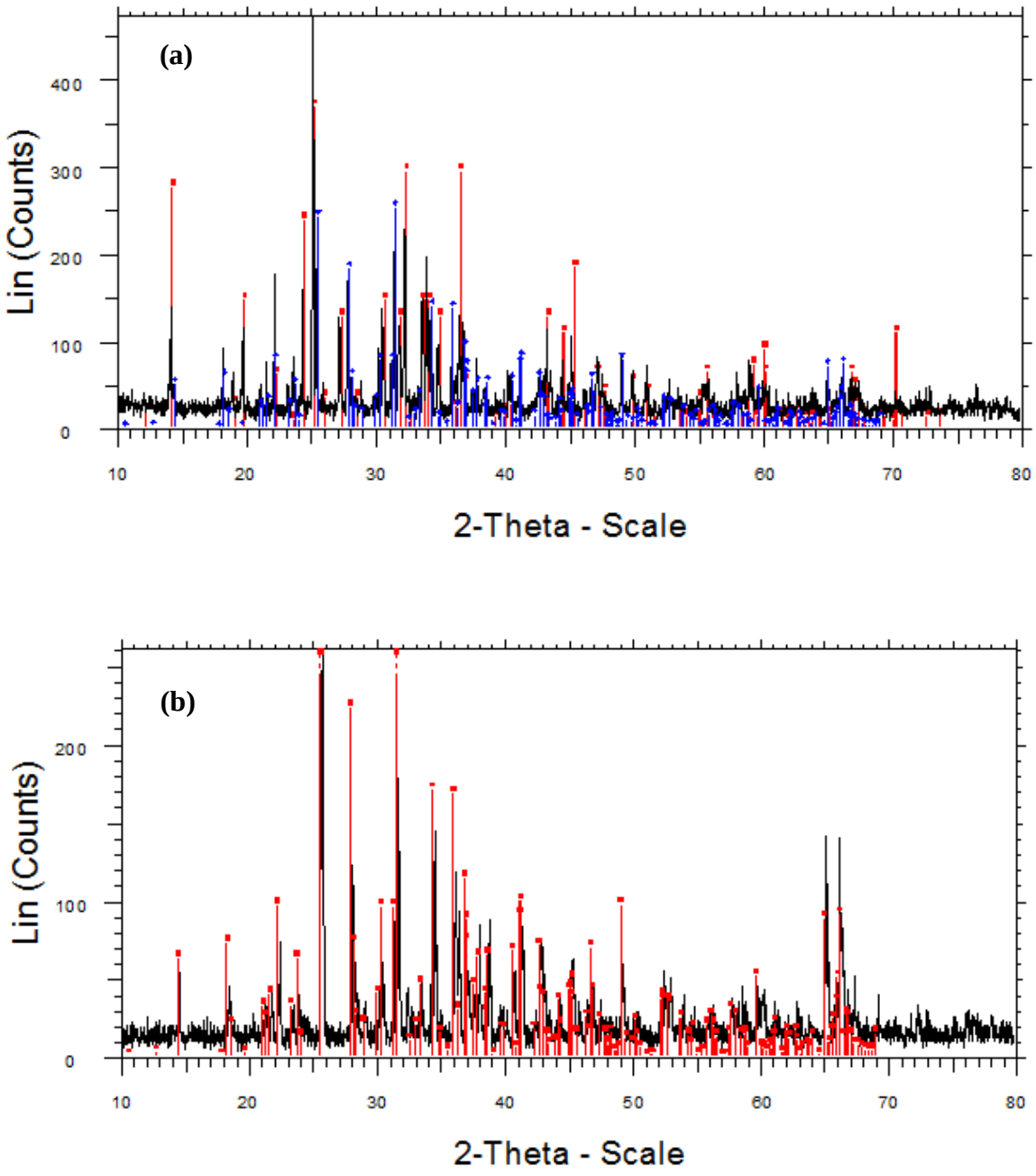

Figure 3.23 The XRD spectra for SA_2 powders with 10 mol% B calcined at (a) 1100°C for the first time and (b) calcined at 1100°C for a third time. In part *a* the red peak labels correspond to $SrAl_4O_7$ (SA_2), and the blue ones to $Sr_4Al_{14}O_{25}$ (S_4A_7). In part *b* the red peak labels correspond to $Sr_4Al_{14}O_{25}$ (S_4A_7).

As mentioned in the experimental part, SA_2 with 0 mol% B cannot be produced at a calcination temperature of 1000°C. Pure SA_2 powders without any boron can be produced only when calcined at 1100°C (Figure 3.22*b*).

At 1000°C, SA_2 powders with boron (10, 20 or 30 mol%) are stable and phase pure. However, when they are re-calcined at 1100°C for once, a second phase appears which is identified as $Sr_4Al_{14}O_{25}$ (S_4A_7) (Figure 3.23*a*). After intermediate grinding and re-calcination for a third time, this second phase dominates, and the SA_2 phase shifts completely to S_4A_7 at 1100°C.

3.3 Thermoluminescence Measurements

3.3.1 Methods for Evaluating the Activation Energy

For this part, implementation of the methods to analyze the glow curve of SA_2 samples will be presented [31]. Due to some technical limitations of the software that runs the TL reader, data points necessitated manual recording, and digitizing the screenshot of the plot by the TL computer.

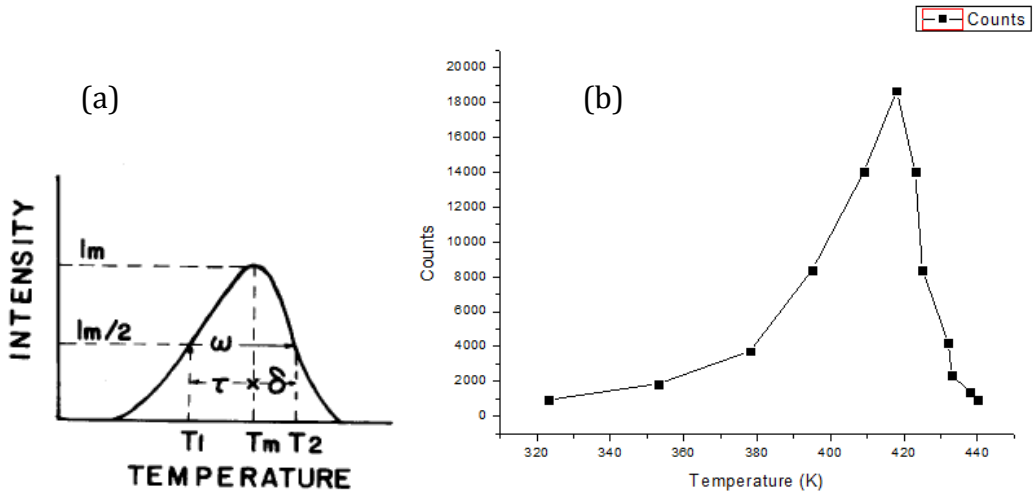

Figure 3.24 Theoretical glow curve with shape parameters indicated (a). One sample glow curve of measured SA_2 powders (b).

In our glow curve (Fig. 3.24*b*), the characteristic parameters are presented in Table 3.1, as described in the theoretical glow curve (Fig. 3.24*a*):

Table 3.1 Shape parameters calculated for our glow curve

	^oK			^oK
T_1	398,62		$\tau = T_m - T_1$	19,38
T_2	424,69		$\delta = T_2 - T_m$	6,69
T_m	418		$\omega = T_2 - T_1$	26,07

3.3.1.1 Determining the Trap Energy Level

This approximation is an empirical one estimated by Urbach [11]. The trap energy in units of eV is defined as:

$$E = T_m/500$$

For our case, $E = 418/500 = 0.836$ eV

3.3.1.1.1 The Initial Rise Method

The **eqn.5** and **eq.6** in the theory chapter will show that intensity, I, is a function of $\exp(-E/k_BT)$ only for the initial rising part of a glow curve, regardless of the order of the de-trapping kinetics. This is why **eqn.5** and **eqn.6** can be generalized such that the kinetic order parameter can be changed with a general order parameter b:

$$I = -dn/dt = s' n^b \exp(-E/k_BT) \qquad \textbf{Eqn.7}$$

Then, Garlick and Gibson suggested a method that at the beginning of the glow peak, plotting $\ln I$ as a function of $1/T$ should give a straight line at this region, and therefore the slope is $-E/k_B$. The corresponding plot for our glow curve is as follows:

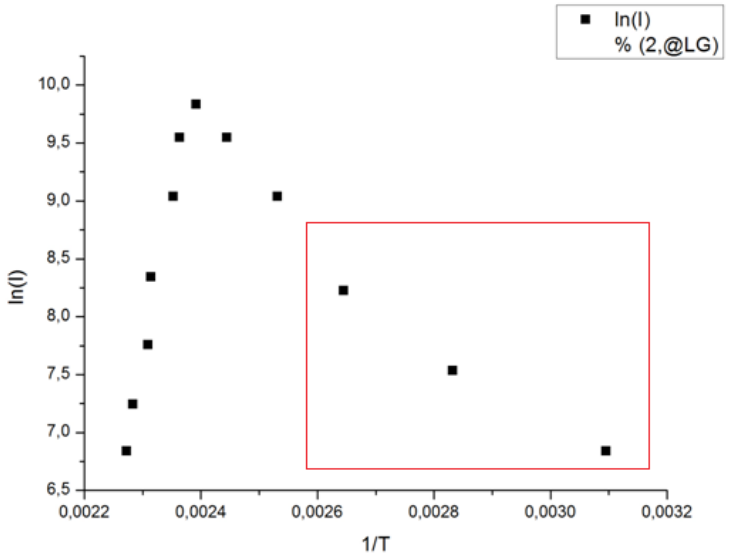

Figure 3.25 ln*I* as a function of 1/*T*

This data was replotted for the first three temperature points and fitted a linear equation. It is basically the magnified version of the red rectangle in Figure 3.25.

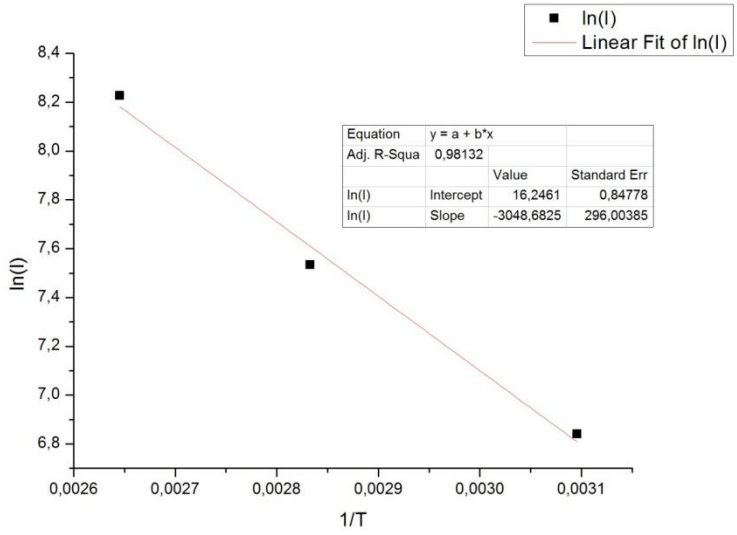

Figure 3.26 The linear fit of the last 3 data points.

The slope of this equation is calculated as -3048.6825. According to Garlick and Gibson, this should be equal to $-E/k_B$ where k_B is the Boltzmann constant $\approx 8.617\ 10^{-5}$ eV-K^{-1}.

Then, E = 3048.68 * 8.617x10^{-5} = 0.2627 eV

3.3.1.1.2 Methods employing the shape parameters of the peak

The shape parameters are shown in the Table 3.2. The methods proposed by Lushchik, Halperin and Braner and Chen can be summarized as follows:

$$E_\alpha = c_\alpha(k_B T_m^2/\alpha) - b_\alpha(2k_B T_m) \qquad \textbf{Eqn.8}$$

Where, $\tau = T_m - T_1$ $\delta = T_2 - Tm$ and $\omega = T_2 - T1$ andα is τ, δ or ω. The values c_α and b_α are given in the following table:

Table 3.2 The values c_α and b_α for different types of shape parameters

	First Order			Second Order		
	τ	**δ**	**ω**	**τ**	**δ**	**ω**
c_α	1,51	0,976	2,52	1,81	1,71	3,54
b_α	1,58 + τ/2	δ/2	1 + ω/2	2 + τ/2	δ/2	1 + ω/2

How to use this table?

Let's calculate the activation energy for a First Order Case, using the second half of the TL glow curve. In this case, we have to use our δ value for which was given as 6.69 K in table1. The corresponding c_α and b_α values are c_α = 0.976 and b_α = 6.69/2 = 3.345. So, the **eqn.8** becomes:

E_α = (0.976)*(8.617 10^{-5}*$(418)^2$/6.69) – 3.345*(2*8.617 10^{-5}*418)

E_α = 1.955 eV.

I calculated all the possible E values using different shape parameters for both first and second order case. The results table is as follows:

	First Order				Second Order		
	τ	**δ**	**ω**		**τ**	**δ**	**ω**
E (eV)	0,36122	1,955	0,4443		0,564	3,6074	1,033

According to this table, first you have to decide which kinetics order your data has. Looking at the Figure 3, we can assume that it is first order kinetics (the plot looks

asymmetric rather than symmetric). Then, we have to decide which portion of the TL curve we would like to use: is it the first half, or second half or the full width at half max? In several papers, it is suggested to use the second half (δ) of the TL curve since there will be saturation during the thermal stimulation in the first half (τ) and due to the asymmetric character of the TL curve, full width at half max (ω) is not as reliable as the second half (δ). Then, we can conclude that by using method 3, our E_α is 1.955 eV.

Considering the inconsistency in the activation energy values calculated via the first three methods, it can be concluded that a more reliable method should be employed, which is the T_m-T_{stop} Method.

3.3.1.1.3 T_m-T_{stop} Method

T_m-T_{stop} method is based on the theory of Garlick& Gibson suggested in 1948 [11]. This theory claims that the maximum temperature of a peak can largely change, when the trap population, *i.e.* the amount of electrons in the traps, is substantially altered. The T_m-T_{stop} technique starts with heating a previously irradiated sample to a temperature, T_{stop}, in the TL instrument, and then the sample is heated in the TL until all the remaining curve is read out by the TL software. The same process is repeated by only increasing the T_{stop} value. McKeever suggests that the resolution is obtained, when the increments between T_{stop} values are 5°C\min [19]. Additionally, the first T_{stop} value should be chosen a little higher than the room temperature, and the last T_{stop} value may be a little lower than the vanishing point temperature value of the glow curve where the electrons in the traps are depleted [20].

For every obtained T_{stop} value, first Tm in the glow curve is recorded and obtained values are plotted as a T_m vs T_{stop} plot. The main aim of this method is to help estimating trap positions in the glow curve. Additionally, it gives information on glow curve kinetics, such as detrapping rates.

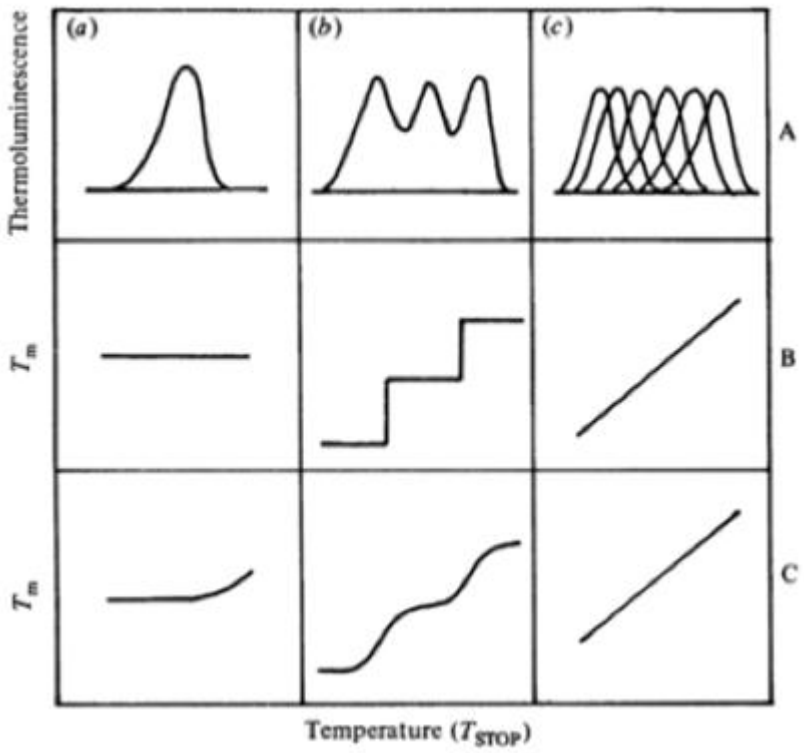

Figure 3.27 Schematic T_m- T_{stop} curves for first-order (column (b)) and second-order (column (c)) thermoluminescence. (a) shows a single glow peak and the corresponding Tm-Tstop curves for first and second-order-kinetics. Column (b) shows the "staircase" shaped T_m-T_{stop} curves which result from overlapping peaks. Closely overlapping, or quasi-continuous distribution of peaks (column *c*) produces a straight line of slope ~1.0. [19].

Figure 3.27 shows different trap distributions in glow curves. In column (a), there is only one Tm value after Tm-Tstop method is applied. This means that there are no hidden peaks under the glow peak. In column (b), there is a stepwise increase in Tm values, the number of plateaus indicates the number of peaks that forms the main glow curve. Column (c) is very similar to column (b), however in column (c) peaks are strongly overlapping. In the figure, row B and C show the kinetic order. Kinetic order becomes an important parameter, since the Glowfit software gives great results in terms of fitting the peak positions obtained by the T_m- T_{stop} method into the glow curve, when the kinetic order is close to one like shown in the column A.

In the first experiment where T_m- T_{stop} method is applied, the T_{stop} values are chosen between 40-238°C with 6°C increments for S_4A_7 with 30 mol% B . As a heating rate, 3°C/min was used, since the TL instrument allowed control over linear heating rates.

Because the TL instrument (Rexon UL-320 TLS system), has difficulty heating linearly above 200°C, if it is not operated 10-12 times, it is important to operate the system at least 10 times without a sample before commencing measurements.

Figure 3.28 shows the T_m- T_{stop} plot of S_4A_7 with 30 mol% B. The reason for picking this sample rather than SA_2 phase is because SA_2 phase glows so weak that this method cannot be employed. Even for this S_4A_7 phase, the T_{stop} values beyond 200°C are excluded, since their T_m values cannot be determined precisely because of the low resolution which will discussed later.

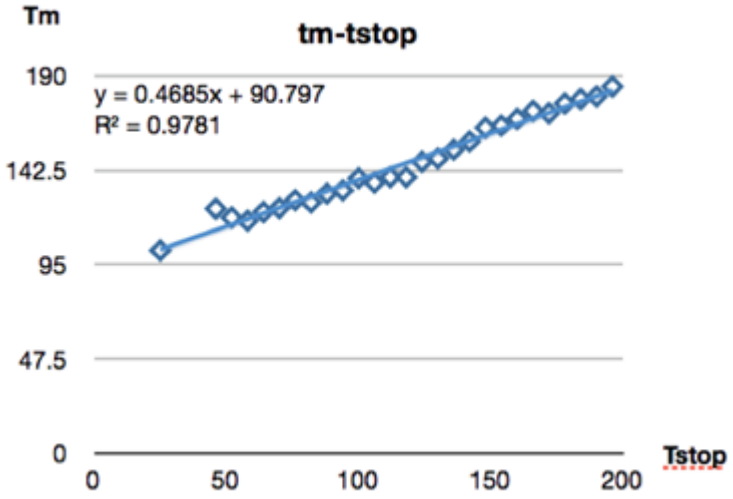

Figure 3.28 T_m- T_{stop} plot for S4A7 with 30 mol% B.

Although this plot looks linear and therefore has more closely overlapping peak characteristics, increasing the resolution of the method by decreasing the increments between T_{stop} values could yield a more stepwise increase between Tm values like demonstrated column (b) in the first figure. Additionally, the plot does not have a slope around 1, as it is supposed to have when the peaks are closely overlapped, such as the case shown in the column (c) of Fig. 3.27.

In order to increase resolution of T_m- T_{stop} method, the increments between T_{stop} values are decreased to 3°C. 365 nm λ UV light is used as an irradiation source, for 3 minutes for every T_{stop} value. For the rest of the measurements, heating rate was chosen to be 3°C and

sample was the same S_4A_7 with 1 mol% Eu, 1 mol% Dy and 30 mol% B sample. The T_m-T_{stop} plot in Figure 3.29 is a proof the importance of the T_{stop} increments in implementing the T_m- T_{stop} method.

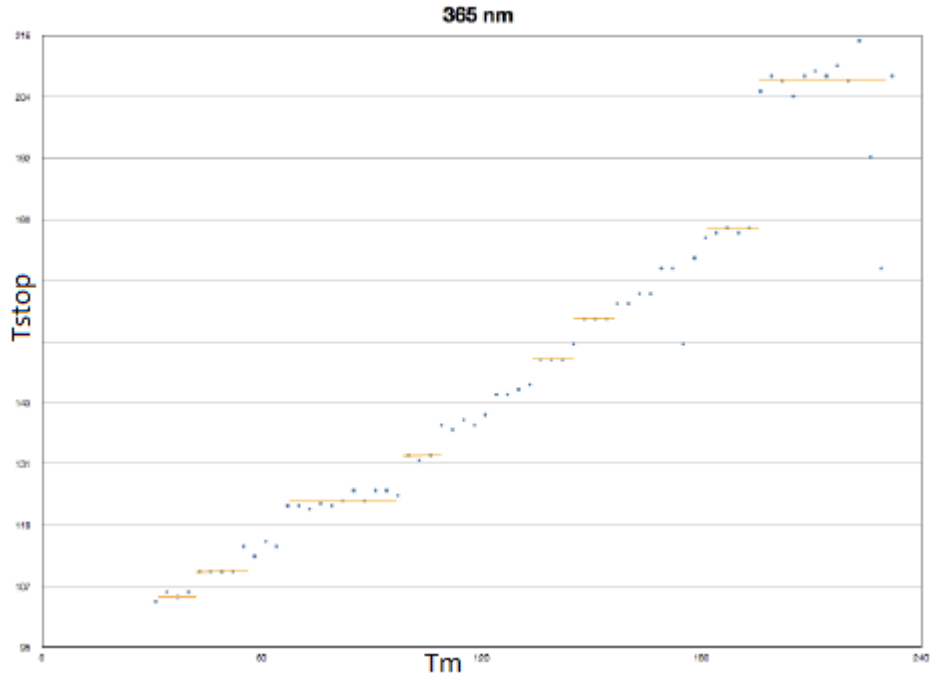

Figure 3.29 T_m- T_{stop} plot for UV irradiation at wavelength of 365 nm.

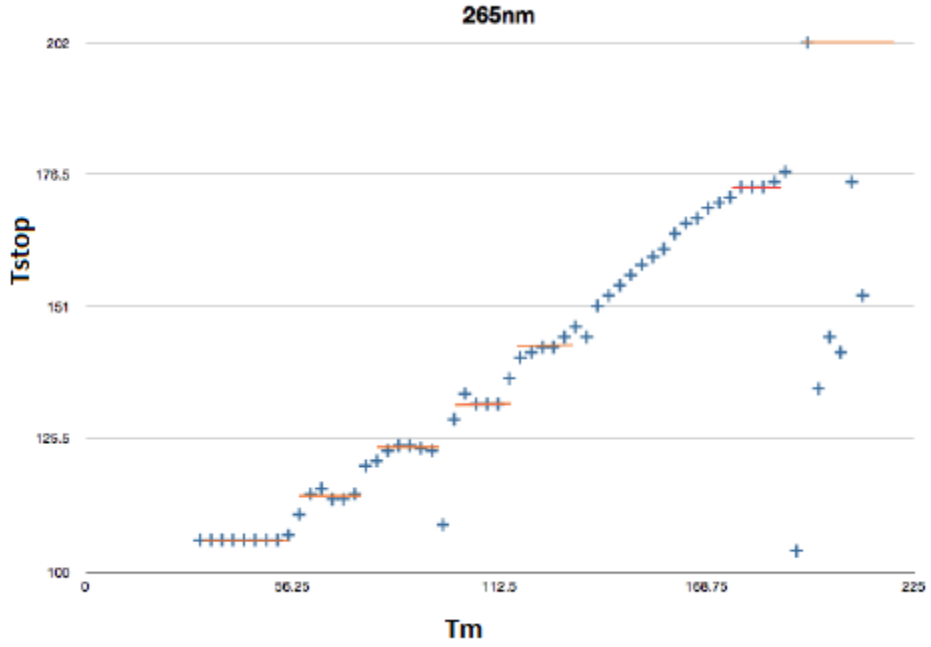

Figure 3.30 T_m- T_{stop} plot for UV irradiation at wavelength of 265 nm.

Unlike the first measurement, T_m- T_{stop} plot in Figure 3.31 shows characteristics of staircase T_m- T_{stop} plots. The eight plateaus indicated by orange line in the plot show the characteristic glow peaks that form original glow peak.

In order to increase resolution at higher T_{stop} values, the number of electrons in the traps should be increased, since more electrons in the traps could yield more powerful phosphorescence, assuming that retrapping rate is constant. UV source with higher energy (λ = 265 nm) is preferred, and the new plot for the UV excitation at this wavelength is shown in Figure 3.30.

This plot is very similar to the previous one obtained with a lower energy excitation source (Figure 3.29). The staircase structure is more prominent in the last experiment which could be a result of higher frequency; however for T_{stop} values that are higher than 200°C, there is an inconclusive decrease in T_m values. Based on the similarity between these two last experiments, it is assumed that there is a plateau around a T_m value of 202°C, which can be seen in the plot that was obtained by using a λ = 365 nm irradiation source.

As mentioned before T_m- T_{stop} method is a method for estimating the trap positions. Plateaus shown in T_m- T_{stop} plot gives characteristic glow peaks that belong to traps. In the last experiment, there are 8 plateaus, which correspond to T_m values of 106°C, 114°C, 124°C, 132°C, 143°C, 174°C and 202°C. Figure 3.31 shows these glow peaks. The titles above the figures indicate from which T_{stop} value the glow peaks were obtained. The first figure belongs to the original glow curve, which was simply obtained by normal thermoluminescence measurement.

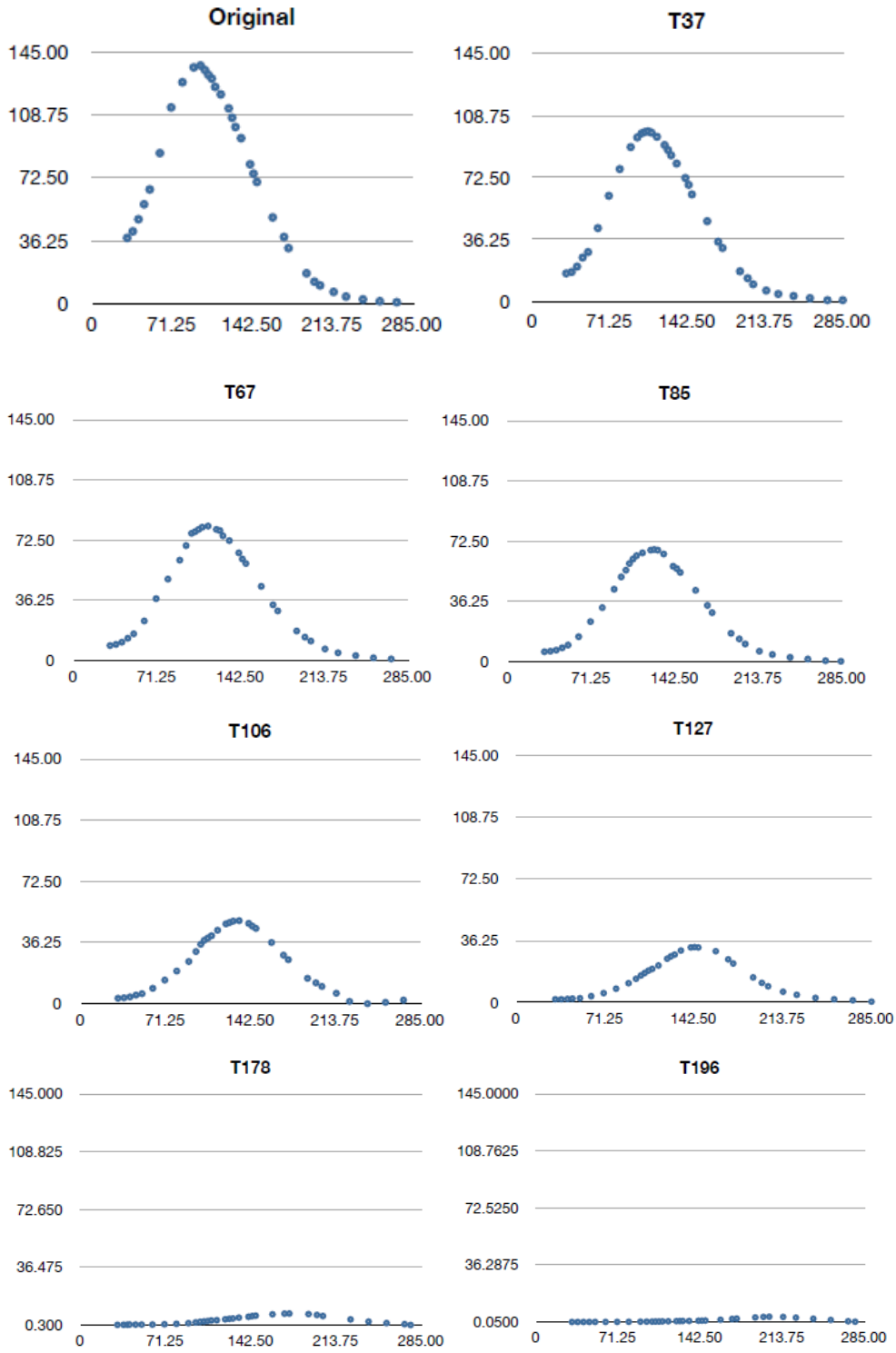

Figure 3.31 Glow peaks correspond to the Tm values which cause a plateau in Figure 3.30.

Using these characteristic glow peaks, one can form the electronic band structure of S_4A_7 with 30 mol % B content by calculating each glow peak's trap depth. However, doing this

may be not a healthy solution in terms of revealing electronic structure. In T_m-T_{stop} method, except the last characteristic glow peak, all other obtained glow peaks should have something in common with the subsequent glow peak. Therefore, common points should be eliminated from each glow peak. In order to that, Fourier transformation looks like a proper way. Some deconvolution trials were performed using Origin 8.0 software, however the results were not meaningful to present here, and therefore a further study on mathematical analysis of these findings should be conducted.

Apart from the analytical study of thermoluminescence glow curves, thermally stimulated luminescence studies were performed on SA_2ED powders with B content in molar percentages—0%, 4%, 8% and 11%—in order to understand the effect of boron on the trapping strength, which may be related to the prolonged de-trapping. Furthermore, to understand the effect of calcination temperature, the measurements were done for the two sets of samples, one calcined at 1000°C (formation of the SA_2 phase) and the other at 1100°C (formation of the S_4A_7 phase). Figure 3.32 shows that the thermoluminescence intensity changes dramatically in boron containing SA_2ED powders, which suggests that boron incorporation has a subtle effect on the activation energies in the trap states. This conclusion is valid for both calcination temperatures.

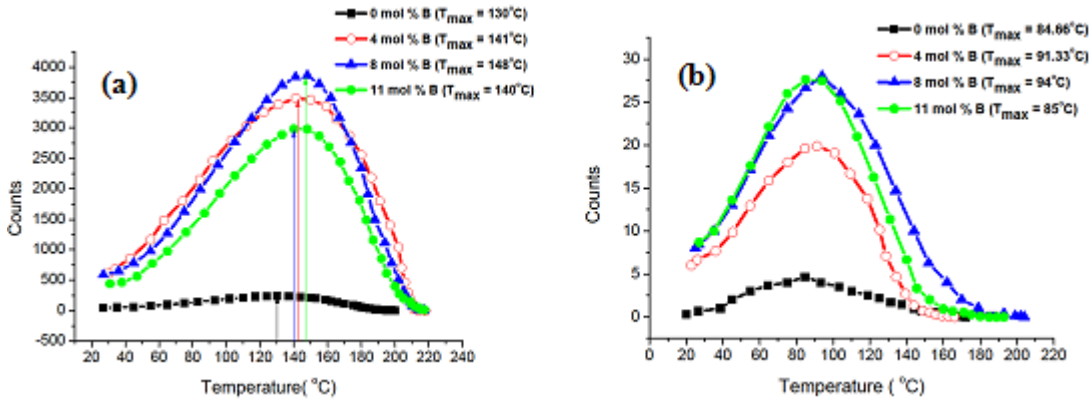

Figure 3.32 The thermoluminescence glow curves for the SA powders calcined at (a) 1100°C and (b) 1000°C containing 0 mol% B (squares), 4 mol% B (empty circles), 8 mol% B (triangles) and 11 mol% B (filled circles).

3.4. Photoluminescence Measurements

The phosphorescence spectra for the SA_2ED and S_4A_7ED powders summarized in Figure 3.33 clearly show a luminescence peak at 2.5 eV. Although the intensity between samples varied too widely to be compared, the duration of the phosphorescence was observed for the SA_2 powders with B molar percentages0%, 4%, 8% and 11% and calcined at 1000 $^{\circ}$C and 1100 $^{\circ}$C, after UV irradiation (λ_{ex} = 365 nm) of the powders for 10 minutes. The afterglow duration for the samples calcined at 1000°C lasted no longer than 20 seconds. In contrast, for the samples calcined at 1100°C, the phosphorescence is remarkably longer. Those which contained boron were still noticeable with the naked eye after 5 hours, whereas the sample with no boron was noticeably bright only for about 5 minutes. The actual boron content did not correlate with the afterglow duration.

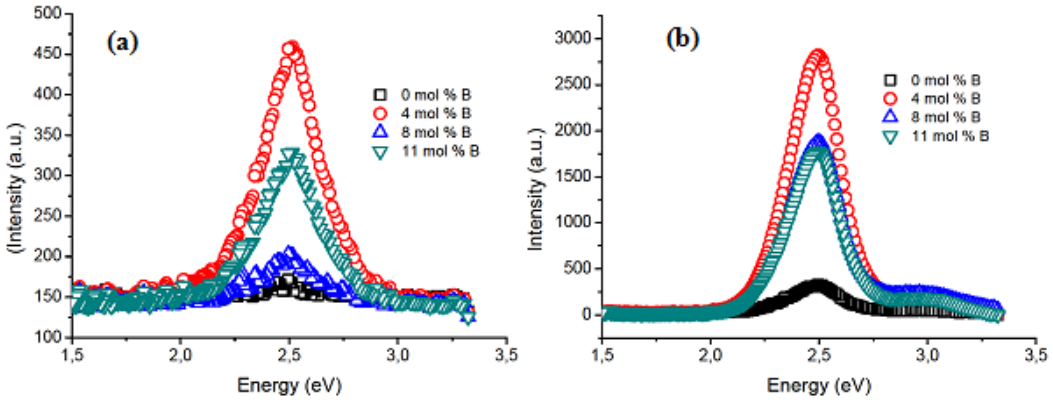

Figure 3.33 Phosphorescence spectra for the SA_2 powders calcined at (*a*) 1000°C and (*b*) 1100°C containing 0 mol% B (squares), 4 mol% B (circles), 8 mol% B (triangles pointing up) and 11 mol% B (downwards triangles).

3.5. Inductively Coupled Plasma Mass-Spectroscopy Measurements

Boron is a small atom that can diffuse into the alumina crucibles during the calcination at elevated temperatures such as 1000 ^{0}C. In case of such a diffusion, the actual boron content of SA powders would be less than calculated. In order to determine this possible boron diffusion, SA powders were calcined in both alumina and platinum crucible which is known to be inert. Furthermore, a lid was placed onto the platinum crucible to prevent losses during the evaporation. Here are the results:

Alumina Crucible	Platinum Crucible
0	0
4.07	4.45
7.931	8.29
11.398	11.398

Figure 3.34 ICP Analysis Results

The amount of B in powders is almost the same both for those calcined in alumina and platinum crucibles. It was shown that B is not reacting with the alumina crucible and since the measured amounts are very close to the calculated B contents, we confirmed that we have the control over the B content in SA phosphors.

Characterizations	SA_2	S_4A_7
XRD peak shifts	✓	
ICP	✓	
ELNES	✓	
PL Spectroscopy	✓	✓
TL Spectroscopy	✓	✓

Figure 3.35 Summary of characterizations.

Figure 3.35 summarizes the characterizations performed so far.

CHAPTER 4. DISCUSSION

Boron has been used as a network former in glasses just like silicon, germanium or phosphorus. Unlike the network modifiers which force the network to be formed around them, network formers link to the oxygen atoms and they are directly incorporated into the network [30].

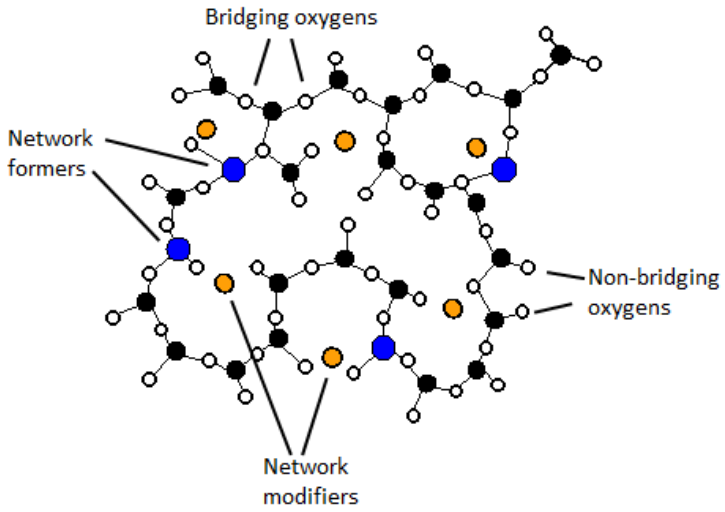

Figure 4.1 Illustration of a glass network

As seen in Figure 4.1, when an oxygen atom is linked to more than 1 cation, it is called a bridging oxygen whereas if this number is 1, which means that this oxygen is not acting like a bridge connecting the structural units, it is a non-bridging oxygen. A network modifier breaks the second bond of the oxygen, turning it into a non-bridging oxygen. However, a network former is coordinated to more than one oxygen, forming the network.

Al atoms are being used as intermediates, which are both network formers and modifiers depending on the glass composition. In SA_2, there are 2 types of Al coordination: 4-fold and 5-fold. When boron enters the lattice in large amounts such as 20 mol %, it might be acting like a network former as it does in glass networks. However, it works as a network modifier in SA lattice. From the ELNES fingerprinting, it is observed that most of the boron occurs in 3-fold coordination inside the lattice, so boron might be entering into the lattice as $(BO_3)^{3-}$ units networking with each other. This might cause boron rich regions to

appear, which explains the non-uniform distribution of the B ELNES signal throughout the different points on the SA_2 particles.

Furthermore, quantitative analysis of the ELNES data showed that whenever there is B signal, there is also a decrease in Al ion signal which suggests that there are less Al ions for these points. As seen in the crystal structure, the Al atoms in the SA_2 lattice are both 4-fold and 5-fold coordinated. The size of a B ion is a few picometers whereas that of 4-fold and 5-fold Al ions is 39 and 48 picometers respectively [22]. It was observed that, when there is no boron incorporation, macroscopically phase pure SA_2 is formed at 1100 ^{o}C. When there is boron even in small amounts such as 5 mol %, SA_2 is not phase pure anymore. A second S_4A_7 phase appears together with SA_2 and after performing multiple calcinations at this temperature; S_4A_7 phase dominates and eventually becomes the only phase. Considering these data, it might be concluded that boron entering into the lattice increases the number of non-bridging oxygens, and therefore increasing the oxygen coordination of Al cations (there are 4-fold and 6-fold coordinated Al atoms in S_4A_7). However, as confirmed by the XRD data, boron cannot form long range networks as it does in a glass structure when it is in SA_2 matrix. Instead, it is possible that boron remains as short-range networked B_2O_3 chunks. As the number of bridging oxygens decrease and the coordination of Al is increased, the new system experiences a phase transformation to maintain the charge balance and SA_2 phase shifts into S_4A_7. As a result, even though boron is a network former itself, B_2O_3 units force the network to be formed around them which means that boron acts as a network modifier in SA_2.

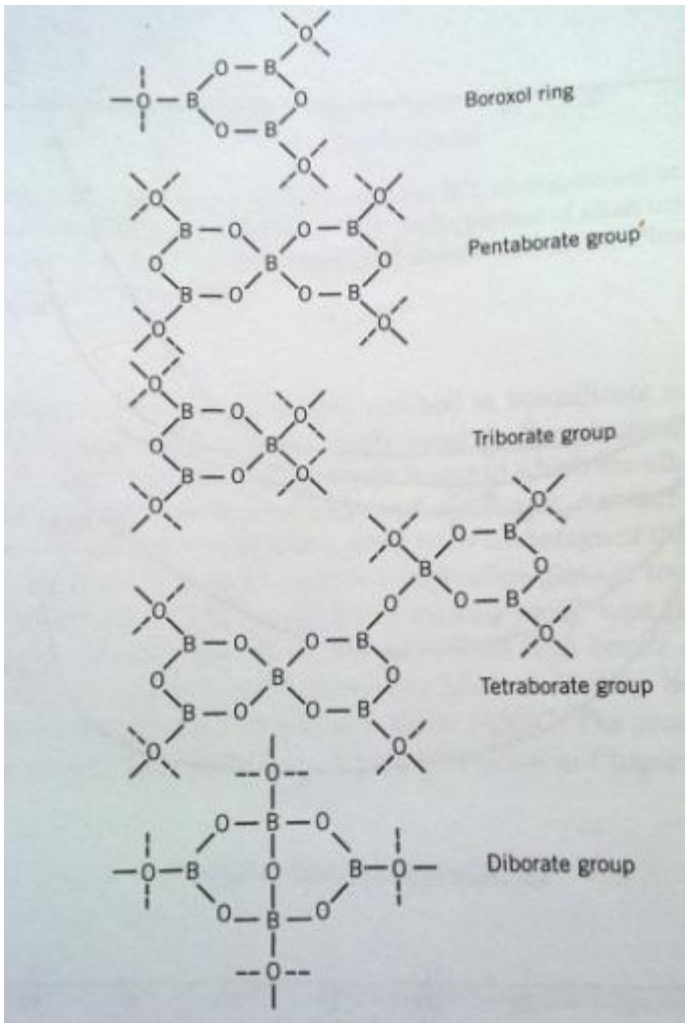

Figure 4.2 Possible structural elements of borate glass [30]

Figure 4.2 shows the possible coordinations for B when it is in network structure. As seen here, some of the boron atoms are 4-fold coordinated. The ELNES fingerprinting of B-*K* edge showed some small distortions in trigonally coordinated B peaks and we proposed that the signal we get might be a combination of both 4-fold and 3-fold coordinated boron. The possibility of boron's forming pentaborate, triborate, tetraborate or diborate groups might explain the 4-fold coordination traces seen in B-*K* edge data.

It was also observed that in S_4A_7 phosphors, even though the powders were not reduced, there was still some phosphorescence in powders with any amount of B. So addition of B causes the reduction of Eu^{3+} to Eu^{2+}. This can again be explained by the network modifying function of $(BO_3)^{3-}$ units which liberate some of the oxygens linked to Eu,

deform the e^- density distribution around Eu, breaking the symmetry which lifts degeneracy. Therefore some of the Eu atoms will experience the same effect as the reduction process causes.

CHAPTER 5. CONCLUSIONS

The effect of boron incorporated into Eu^{2+} and Dy^{3+} co-doped (1 mol% each) SA_2 and S_4A_7 phosphors was investigated. Our main goal was to understand the electronic structure when boron is incorporated into the SA crystal lattice, specifically for the SA_2 phase. However, inspection of different calcination temperatures revealed a second phase (S_4A_7) evolving from the same stoichiometric mixture, which was prepared to produce SA_2 phase. Optical measurements showed that incorporation of boron increased the phosphorescence intensity and afterglow duration dramatically for both phases. However, S_4A_7 phase has vast superiority over the SA_2 phase, such as easier reduction, being water-soluble (SA_2 phase is highly hygroscopic), up to 7 hours of phosphorescence whereas it is 20 minutes for SA_2 phase and emission intensity.

ELNES studies showed that boron inside the SA_2 crystal occurs as a mixture of 3-fold and 4-fold coordinations. Quantitative study of the ELNES spectra showed that 3-fold coordinated boron atoms might be locally replacing Al atoms sitting in 4-fold and/or 5-fold coordinations. However, macroscopically, stoichiometry is preserved, indicating that the replaced Al atoms may be accumulating locally in other locations.

Preliminary XRD studies showed promising results, however repeating of the same measurements gave inconclusive data, most probably due to the recent maintenance work in the instrument and these studies should definitely be repeated.

In conclusion, the characterizations discussed in this work helped us understanding some of the mysteries we were looking for. Further studies in collaboration with Joseph Stefan Institute, Ljubljiana, Slovenia and Max-Planck Institute, Stuttgart, Germany is being conducted.

CHAPTER 6. FUTURE WORK

Since there is still much to learn, this research inspires some new questions to be answered. Following research can bring us many steps closer to the big picture:

1- The critical concentration of B to form enough non-bridging oxygens for $SA_2 \rightarrow S_4A_7$ transition should be detected.

2- In order to better understand the role of Dy, emission and absorption spectra of samples with and without Dy dopants should be acquired so that if there is an energy transfer from Dy to Eu, it can be detected.

3- The TL data should still be mathematically analyzed in order to get trap depth information

REFERENCES

1. Nemoto& Co., Ltd. *Long Afterglow Phosphorescent pigment LumiNova*. Retrieved June 27, 2011 from http://www.nemoto.co.jp/en/products/luminova/goods.html.
2. Y. Murayama, in, S. Shionoya, W.M. Yen (Eds.), "Phosphor Handbook",CRC Press, Boca Raton, FL, USA, 651, (1999).
3. Nag, A. et al., "The mechanism of long phosphorescence of $SrAl_{2-x}B_xO_4$ ($0 < x < 0.2$) and $Sr_4Al_{14-x}B_xO_{25}$ ($0.1 < x < 0.4$) co-doped with Eu^{2+} and Dy^{3+}", ***Materials Research Bulletin***, 39,331-342, (2004).
4. Chang, C. et al., "Preparation of long persistent $SrO.2Al_2O_3$ ceramics and theirluminescent properties", ***Journal of Alloys and Compounds***, 348, 224-230, (2003).
5. Yuan, H. B. et al., "The Long-Persistent Photoconductivity of $SrAl_2O_4:Eu^{2+}$, Dy^{3+} Single Crystals", ***Journal of Electrochemical Society***, 147 (8), 3154-3156, (2000).
6. Chen, I-Cheng et al., "Sol-gel synthesis and the effect of boron addition on the phosphorescent properties of $SrAl_2O_4:Eu^{2+},Dy^{3+}$ phosphors", ***J. Mater. Res***., 16, 644-651, 2001.
7. Eskin, M. G. et al., "Effect of Boron on Processing and PhosphorescenceBehavior of $SrAl_4O_7$ (SA_2) Co-doped with Eu^{2+} and Dy^{3+}", **Mater. Res. Soc. Symp. Proc**. 1309, (2011).
8. Egerton, R. F., "Electron energy-loss spectroscopy inthe TEM", ***Rep. Prog. Phys***. 72, 016502, (2009).
9. Williams, D. B. and Carter, C. B., "Transmission Electron Microscopy: A Textbook for Materials Science", **Springer**, New York, 679-683, (2009).
10. Katsumata, T. et al., "Characterization of trap levels in long-duration phosphor crystals", **Journal of Crystal Growth**, 237-239, 361-366, (2002).
11. Furetta, C. et al., "Review: Models in Thermoluminescence", **Journal of Materials Science**, 39, 2277-2294, (2004).

12. Sakka, Sumio,. “Handbook of Sol-Gel Science and Technology: Processing, Characterization and Applications”, ***Kluwer Academic Publishers***, New York, 77-78. (2004).
13. Uluc, Vanya,. “Synthesis and Characterization of Phosphorescent Strontium Aluminate Compounds”, ***Sabanci University***, Istanbul, Masters Thesis, Available from Sabanci University Research Database, ID:13777, 29-31, (2008).
14. Sauer H. et al., “Determination of Coordination’s and Coordination-Specific Site Occupancies by Electron Energy-Loss Spectroscopy: An Investigation of Boron-Oxygen Compounds”, ***Ultramicroscopy***, 49, 198-209, (1993).
15. Garvie, Lauerence A. J. and Buseck, Peter R., “Parallel Electron Energy-Loss Spectroscopy of Boron in Minerals”, ***Reviews in Mineralogy and Geochemistry***, 33;1, 821-843, (1996).
16. Egerton R. F., “Electron Energy Loss Spectroscopy in the Electron Micriscope”, ***Plenum Press, New York***, 272-282, (1996).
17. Bryson, R. et al., “Chemical Information from Electron-Energy-Loss Near-Edge Structure. Core Hole Effects in the Beryllium and Boron K-Edges in Rhodizite”, ***Journal of Physical Chemistry***, 92, 962-966, (1988).
18. Bouchet, D. et al.,"Experimental study of ELNESat grain boundaries in alumina:intergranular radiation damage effects on Al-L23 and O-K edges", ***Ultramicroscopy***, 96, 139-152, (2003)
19. McKeever, S. W. S., “Thermoluminescence of Solids”, ***Cambridge University Press***, Cambridge, (1985).
20. Sharma, S. K. et al., “Luminescence studies on the blue–green emitting Sr4Al14O25:Ce3+ phosphor synthesized through solution combustion route”, ***Journal of Luminescence***, 129-2, 140-147, (2009).
21. Sariyamurthy, N. and Panigrahi, B. S., “Effects of non-stoichiometry and substitution on photoluminescence and afterglow luminescence of Sr4Al14O25:Eu2+, Dy3+ phosphor”, ***Journal of Luminescence***, 128, 1809-1814, (2008).

22. Nag, A. and Kutty, T.R.N., "Role of B2O3 on the phase stability and long phosphorescence of SrAl2O4:Eu, Dy", ***Journal of Alloys and Compounds*** 354, 221-231, (2003)

23. Haranath, D. et al,; "Role of boric acid in synthesis and tailoring the properties of calcium aluminate phosphor", ***Materials Chemistry and Physics*** 101, 163-169, (2007)

24. Haranath, D. et al.; "Optimization of boric acid content in developing efficient blue emitting, long persistent phosphor", ***J. Phys. D***., 38, 371-375, (2005)

25. Clabau, F. et al.; "On the phosphorescence mechanism in SrAl2O4:Eu2+ and its codoped derivatives", ***Solid State Sciences*** 9, 608-612, (2007)

26. Chang, C. et al; "Preparation of long persistent SrO.2Al2O3 ceramics and their luminescent properties", ***Journal of Alloys and Compounds*** 348, 224-230, (2003)

27. Pelle, F et al; "Optically stimulated luminescence of persistent luminescence materials", ***Journal of Luminescence*** 119-120, 64-68, (2006)

28. Luitel, H. N. et al; "Luminescent properties of Cr3+ doped SrAl14O25: Eu/Dy blue-green and red phosphor", ***Optical Materials***, 31, 1200-1204, (2009)

29. Clabau, F. et al; "Mechanism of phosphorescence appropriate for the long-lasting phosphors Eu2+-doped SrAl2O4 with Codopants Dy3+ and B3+", ***Chem. Mater.*** 17, 3904-3912, (2005)

30. Chiang, Y., Birnie, D. and Kingery, W. D.; "Physical Ceramics; Principles for Ceramic Science and Engineering", ***John Wiley & Sons Inc.***, 1997, 87-93.

31. Chen, R., Review: "Methods for kinetic analysis of thermally stimulated processes", ***Journal of Materials Science*** 11, 1521-1541, (1976)